

RESEARCH

Open Access



Acid-responsive aggregated carrot-derived nanoantioxidants alleviate oxidative stress and restore osteoblast activity

Jiao Peng^{1,4}, Rongyan Liu^{1,4}, Junyi Xu^{1,4}, Yingjuan Yao^{1,4}, Beibei Li^{1,4}, Dengke Chen^{1,4}, Zhuangpeng Chang^{1,4}, Rui Zhao^{1,4}, Yanlin Feng^{3*}, Ruigang Hou^{1,4*}, Min Lee^{2*} and Xiao Zhang^{1,4*}

Abstract

Background Excessive generation of reactive oxygen species is a hallmark of the osteoporotic bone microenvironment, which leads to the damage of mitochondrial function and the deactivation of osteoblasts. Fruits and vegetables are rich sources of antioxidants, which play a key role in scavenging free radicals and maintaining the body's homeostasis.

Results Herein, we have developed a type of vesicle coming from carrots as nanoantioxidants to counteract oxidative stress and restore the vitality of osteoblasts for reversing osteoporosis. Nanovesicles are derived from carrot juice using a straightforward extrusion method, resulting in stable membrane structures containing various lipids and homologous active phytochemicals. Nanovesicles can maintain stable structures under normal physiological conditions (pH 7.4) and transform into aggregates in response to the acidic extracellular pH of osteoporosis (pH 4.0). As anticipated, nanovesicles can passively target and aggregate to osteoporotic bone, ease oxidative stress, restore mitochondrial function, promote osteoblastogenesis, and reduce bone loss in osteoporotic mice.

Conclusions This work presents the first demonstration of nanovesicles derived from carrots as novel nanoantioxidants to realize the long-awaited osteogenesis, contributing to the exploration of a brand-new idea for reversing osteoporosis.

Keywords Carrot-derived nanoantioxidants, Passive targeting to bone tissue, Acid-triggered aggregation, Restoration of mitochondrial function, Restore osteoblast activity, Osteoporosis therapy

*Correspondence:

Yanlin Feng

feng@sxmu.edu.cn

Ruigang Hou

houruigang@sxmu.edu.cn

Min Lee

leemin@ucla.edu

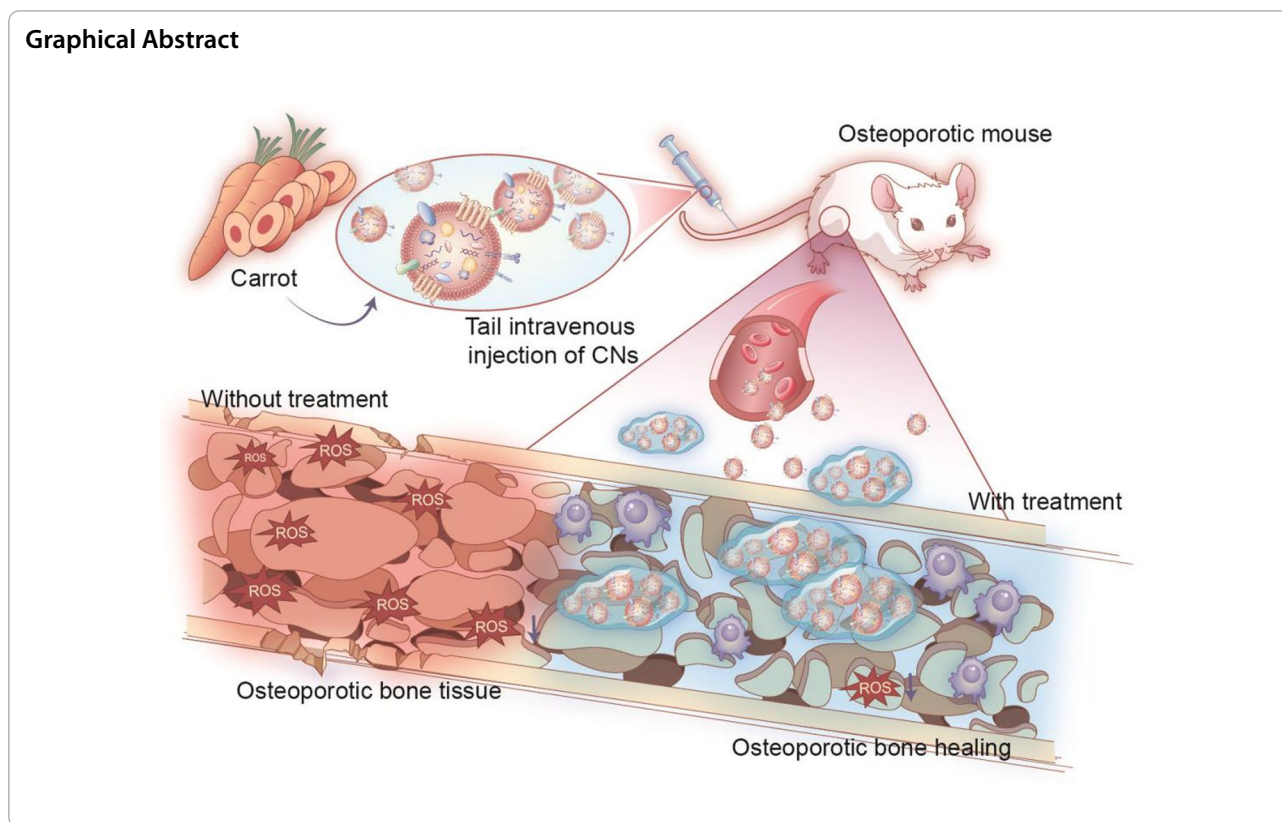
Xiao Zhang

xiao.zhang1@hotmail.com; zhangxiao24@a.sxmu.edu.cn

Full list of author information is available at the end of the article



© The Author(s) 2025. **Open Access** This article is licensed under a Creative Commons Attribution-NonCommercial-NoDerivatives 4.0 International License, which permits any non-commercial use, sharing, distribution and reproduction in any medium or format, as long as you give appropriate credit to the original author(s) and the source, provide a link to the Creative Commons licence, and indicate if you modified the licensed material. You do not have permission under this licence to share adapted material derived from this article or parts of it. The images or other third party material in this article are included in the article's Creative Commons licence, unless indicated otherwise in a credit line to the material. If material is not included in the article's Creative Commons licence and your intended use is not permitted by statutory regulation or exceeds the permitted use, you will need to obtain permission directly from the copyright holder. To view a copy of this licence, visit <http://creativecommons.org/licenses/by-nc-nd/4.0/>.



Introduction

Osteoporosis is a systemic bone metabolism disorder characterized by low bone density and the deterioration of microarchitecture, resulting in reduced bone strength and an elevated risk of fractures [1–4]. The disruption of homeostasis between bone formation and bone resorption is the primary cause of osteoporosis, which is exacerbated by the rapid growth of aging populations worldwide [5, 6]. The conventional management of bone osteoporosis typically involves systemic drug administration and hormonal therapy but is limited by multiple adverse effects (e.g., varying degrees of liver and kidney damage, and gastrointestinal adverse reactions) [7]. Hence, there is an urgent need to explore new therapeutic strategies for the efficient treatment of osteoporosis. Over the past decades, more and more researchers have suggested that aging and more than 100 chronic degenerative diseases (such as atherosclerosis, diabetes, and neurodegenerative disorders) are associated with oxidative stress, which results from an imbalance between the production of free radicals and body's antioxidative defense system [8–13]. It's worth noting that oxidative stress plays a momentous role in osteoporosis [14–19]. Excessive generation of reactive oxygen species (ROS) including hydroxyl radicals ($\cdot\text{OH}$), hydrogen peroxide (H_2O_2), and superoxide ($\text{O}_2^{\cdot-}$) have been reported to accumulate

in mitochondria [20, 21]. The dysfunction of mitochondria due to oxidative stress causes osteoblast apoptosis, which prominently impedes osteogenesis [22–25]. Therefore, the development of novel antioxidants that reprogram mitochondrial function and prevent apoptosis has the potential to promote osteoblast osteogenic differentiation as a treatment strategy for osteoporosis.

Fruits and vegetables are rich sources of antioxidants, which play a key role in scavenging free radicals and maintaining the body's homeostasis [26–29]. However, the clinical application of natural antioxidants is limited because of their small molecular weight, low yield, complex purification process, instability, and poor bioavailability [30–33]. Recently, nanovesicles derived from plants have drawn much attention as potential therapeutic candidates, on account of their abundant resources, low immunological risk, and biosafety profiles [34–42]. Up till now, some nanovesicles containing various bioactives (including proteins, lipids, mRNA, and microRNA) have been extracted from fruit and vegetables, such as grapes, lemon, and grapefruit for treating cancer and inflammation [43–47]. More importantly, these nanovesicles also contain a range of antioxidant agents, such as flavonoids and polyphenols, which could be shielded by the lipid bilayer membrane from rapid oxidation and degradation [43, 48]. In consequence, nanovesicles derived from

plants are expected to become a new generation of nano-antioxidants, regulating osteoblast cell fate and reversing osteoporosis.

Life experience has demonstrated that carrots are rich in carotenoids, vitamins, and other nutrients, which have been isolated to alleviate oxidative stress but constrained by high dose requirements, and nonspecific targeting *in vivo* [49]. Nanovesicles derived from carrots have been isolated as novel antioxidants to regulate cardiomyoblasts and neuroblastoma cells [50]. However, it has not been reported whether carrot-derived nanovesicles, considered a new generation of antioxidants, can reverse osteoporosis by influencing the fate of osteoblasts. Herein, we selected an extrusion approach to obtain nanovesicles from carrots containing various bioactive substances (e.g., proteins, lipids, organic oxygen compounds, and organic acids). These carrot-derived nano-antioxidants (CNs) displayed excellent stability, good biocompatibility, and outstanding oxidation resistance (Scheme 1). As anticipated, multifunctional CNs as novel nanoantioxidants could triumphantly overcome cell membrane barriers and reduce ROS, thereby inhibiting apoptosis for osteoblast proliferation and osteogenic differentiation *in vitro*. Thanks to the non-continuous bone marrow capillaries characterized by substantial gaps between endothelial cells and canaliculi channels within osteon structure, our nanoantioxidants could passively target and accumulate into bone tissue under the acidic microenvironment [51–53]. Last but not least, these tailor-made CNs could ameliorate oxidative stress, restore mitochondrial function, reduce osteoblast apoptosis, and promote bone reconstruction with excellent biosafety for efficient treatment of postmenopausal osteoporosis via the mitogen-activated protein kinase (MAPK) signaling pathway. This work presented the first demonstration of nanovesicles derived from carrots as novel nanoantioxidants to realize the long-awaited osteogenesis, contributing to the exploration of a brand-new idea for reversing osteoporosis.

Materials and methods

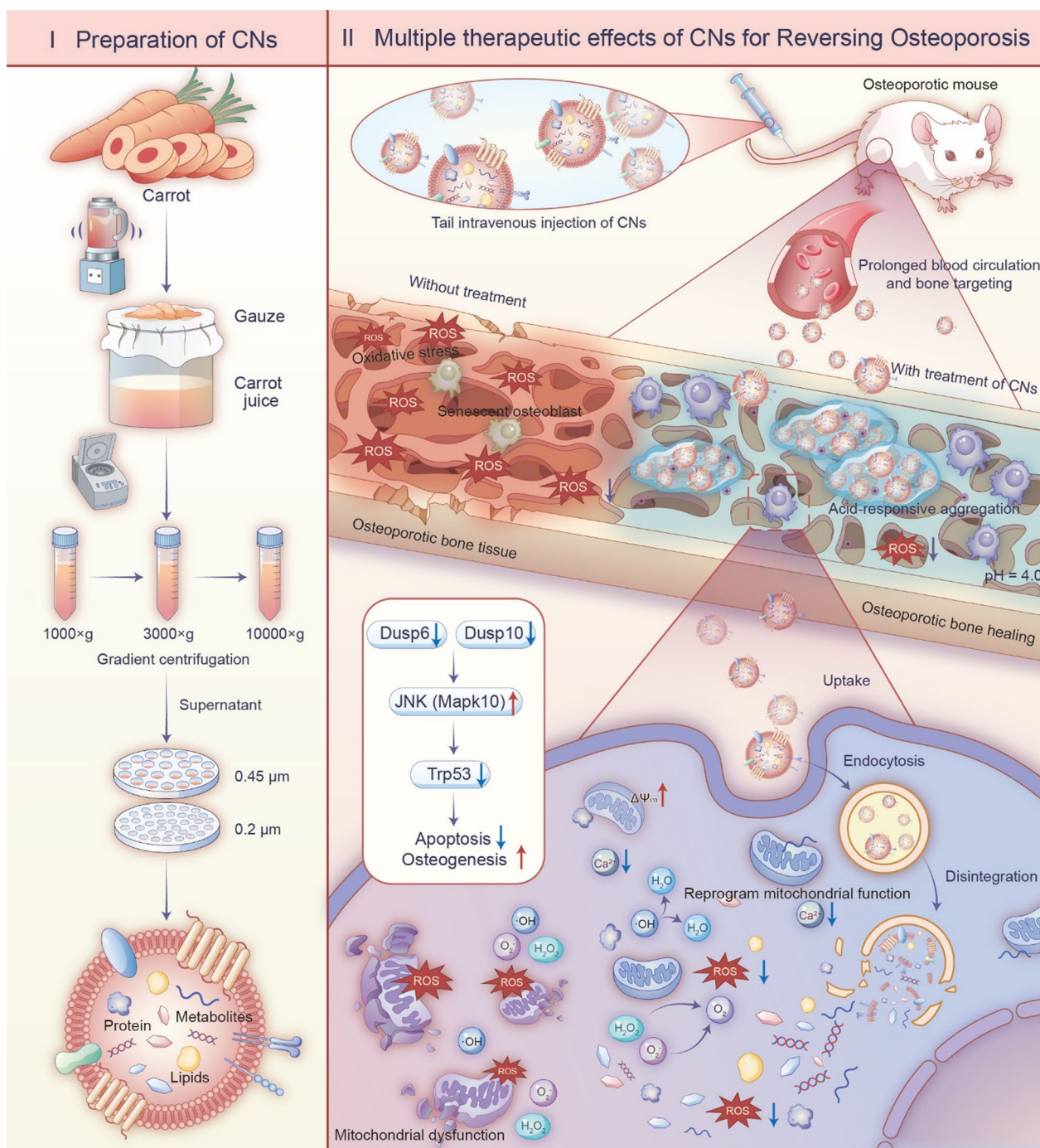
Materials

Erucamide (Eru), fructose (Fru), and quinic acid (QA) were purchased from Aladdin Biotechnology Co., Ltd (Shanghai, China). Chlorpromazine was supplied by Macklin Biotechnology Co., Ltd (Shanghai, China). Cytochalasin D and amiloride were purchased from Good Laboratory Practice Bioscience Technology (GLP-BIO, USA). 2,7-dichlorofluorescein diacetate (DCFH-DA), β -cyclodextrin, BCIP/NBT Alkaline Phosphatase (ALP) Color Development Kit, Hydrogen Peroxide Assay Kit, Reactive Oxygen Species Assay Kit, Calcium Colorimetric Assay Kit, and 3, 3'-diocetadecyloxycarbocyanine

perchlorate (DiO) fluorescent dye and Mitochondria Tracker Red Chloromethyl-X-rosamine (Mito Tracker CMXRos) dye were obtained from Beyotime Biotechnology Co., Ltd (Shanghai, China). Exosome Fluorescent Labeling Dye (DiR) was purchased from Umibio (Shanghai, China). AlamarBlue™ HS Cell Viability Reagent was purchased from Thermo Fisher Scientific (USA). BCA Protein Assay Kit, Hoechst 33342 stain solution, Alizarin Red S (ARS) Solution (0.2%, pH 8.3), Dihydroethidium (DHE) fluorescence probe, and \cdot OH Scavenging Capacity Assay Kit were purchased from Solarbio Science & Technology Co., Ltd (Beijing, China). The Seahorse XF Cell Mitochondria Stress Test Kit was purchased from Agilent Technologies, Inc. (Santa Clara, CA). The Superoxide dismutase (SOD) Assay Kit was purchased from Nanjing Jiancheng Bioengineering Institute (Nanjing, China). Glycerol monostearate (GMS) and the Total Antioxidant Activity (T-AOC) Assay Kit were purchased from Shanghai Yuanye Bio-Technology Co., Ltd (Shanghai, China). Annexin V-FITC Apoptosis Detection Kit was purchased from Dojindo Molecular Technologies, Inc. (Kumamoto, Japan). Terminal deoxynucleotidyl transferase 2-deoxyuridine 5-triphosphate nick end labeling (TUNEL) Apoptosis Detection Kit and Mitochondrial Membrane Potential Assay Kit were purchased from Abbkine Scientific Co., Ltd (Wuhan, China). M5 HiPer Total RNA Extraction Reagent, M5 Super quantitative Polymerase Chain Reaction (qPCR) Kit with gDNA remover, and 2 \times Realtime RCR Supermix (SYBRgreen, with anti-Taq) were obtained from Mei5 Biotechnology Co., Ltd (Beijing, China). Dulbecco's modified eagle medium (DMEM) and fetal bovine serum (FBS) were purchased from Gibco (USA). 4% paraformaldehyde solution, hematoxylin and eosin (H&E) staining solution, and horseradish peroxidase (HRP)-conjugated secondary antibody were purchased from Servicebio Biotechnology Co., Ltd (Beijing, China). Masson trichrome staining solution was purchased from BOMEI Biotechnology Co., Ltd (Hefei, China). The antibody of Dual specificity phosphatase 10 (Dusp10) was obtained from BIOS S Biotechnology Co., Ltd (Beijing, China). Jun N-terminal kinases (JNK) Polyclonal antibody was obtained from Sanying Biotechnology Co., Ltd (Wuhan, China).

Isolation and characterization of CNs

Carrot was purchased from the local vegetable market. Firstly, the carrots were washed with distilled water and peeled. Then, 50 g of carrot cubes were mixed with 75 mL ice-cold phosphate buffer solution (PBS) and squeezed by a high-speed blender to obtain juice. The juice was centrifuged at 1000 \times g for 20 min and 3000 \times g for 20 min to remove large fibers. The obtained supernatant was further centrifuged at 10,000 \times g for 40 min at 4 °C and



Scheme 1. Schematic representation of carrot-derived nanoantioxidants, including preparation of CNs, passive targeting and accumulation in bone tissue acidic microenvironment, reducing oxidative stress, reprogramming of osteoblast mitochondrial function, and promotion of osteogenic differentiation, ultimately contributing to the reversal of osteoporosis

then extruded through the 0.45 and 0.2 μm Millipore filter membrane successively. The concentration of CNs was determined by detecting the protein concentration using a BCA protein quantification assay kit. The size distribution and zeta potential of CNs were measured

by dynamic light scattering (DLS) analysis using a Zetasizer Nano-Zs (Malvern Instruments, UK). The morphology of CNs was determined by transmission electron microscopic (TEM, JEOL JEM-2100Plus, 200 kV). The particle size and concentration of CNs were analyzed via

nanoparticle tracking analysis (NTA) with the Zetaview-PMX120-Z (Particle Metrix, Meerbusch, Germany) and corresponding software Zeta View (Version 8.05.14 SP7).

Stability evaluation of CNs

To evaluate the physiological stability of CNs under different conditions, the CNs were dispersed in PBS buffer at varying pH levels (pH 7.4 and 4.0) and incubated at 37 °C. Subsequently, the size distribution and zeta potential were detected using DLS at different time points. Besides, in order to test the storage stability of CNs at different temperatures, CNs were dispersed in PBS (pH 7.4) and stored separately at 4, – 20, and – 80 °C for the measurement of the zeta potential, size distribution, and protein content every week. The protein content of the CNs prepared from different batches of carrots by the same method in the above was quantified using the BCA assay kit to detect batch stability of CNs. Measurements of CNs in different groups were taken in triplicate, and the results were averaged.

Preparation and characterization of carrot-derived exosomes (CEs)

CEs were prepared by ultracentrifugation method. Briefly, the carrot juice was centrifuged at 1000×g for 20 min, 3000×g for 20 min, and 10,000×g for 40 min in succession, and extruded through the 0.45 and 0.2 μm filter membrane. The supernatant was centrifuged at 150,000×g for 2 h to collect CE pellet by PBS. The size distribution and zeta potential of CEs were measured by DLS and the protein content of CEs was determined by BCA protein quantification assay kit. The total antioxidant capacity of CNs and CEs at the same mass concentration were measured by the 2, 2'-casoin-bis (3-ethylbenzthiazoline-6-sulfonic acid) diammonium salt (ABTS⁺) method described below.

Quantitative proteomics

Proteomic analysis was conducted by Shanghai Zhongke New Life Biotechnology Co., Ltd. The proteins were separated on 4–20% sodium dodecyl sulfate–polyacrylamide gel electrophoresis (SDS-PAGE) gel at a constant voltage of 180 V for 45 min. Protein bands were visualized using Coomassie Blue R-250 staining. The peptides from each sample were analyzed by a TIMSTOF mass spectrometer (Bruker) connected to an Evosep One system liquid chromatography (Denmark) in the data-independent acquisition (DIA) mode. Protein subcellular localization was predicted by the multi-class SVM classification system CELLO (<http://cello.life.nctu.edu.tw/>). Gene Ontology (GO) terms were mapped, and sequences were annotated using the software program Blast2GO. The studied proteins were blasted against the online Kyoto encyclopedia

of genes and genomes (KEGG) database (<https://www.genome.jp/kegg/>) to retrieve their KEGG orthology identifications and were subsequently mapped to pathways in KEGG.

High-resolution untargeted metabolomics

UHPLC-Q-TOF-MS (ultrahigh-performance liquid chromatography equipped with quadrupole time-of-flight mass spectrometry) was used to detect metabolites in CNs. After slowly thawing the samples at 4 °C, the appropriate amount of samples was added to a pre-cooled solution of methanol, acetonitrile, and water (2:2:1, v/v). The mixture was then vortexed, subjected to low-temperature ultrasound for 30 min, and left to stand at – 20 °C for 10 min. After centrifugation at 14,000×g and 4 °C for 20 min, the supernatant was collected and dried under vacuum. During mass spectrometry, 100 μL acetonitrile solution (acetonitrile: water = 1:1, v/v) was added to redissolve, vortex, and centrifuge at 14,000×g at 4 °C for 15 min. The supernatant was sampled for analysis. Analyses were performed using a UHPLC (1290 Infinity LC, Agilent) coupled to a quadrupole time-of-flight (AB Sciex Triple TOF 6600).

Preparation of mimic CNs (MCNs)

MCNs were prepared using the membrane-sonication method. According to the results of the metabolomic analysis, the four main components were selected. Glycerol monostearate, erucamide, and quinic acid for CNs equivalent were dissolved collectively in chloroform/absolute ethanol solutions (1:1, v/v). After the solvent evaporated, the fructose was dissolved in PBS to resuspend the dried film layer. The MCNs were then obtained by sonication using an ultrasonic crusher. When GMS, Eru, QA, and Fru were treated as a single component, their content was equal to that of each component in the MCNs. Detailed data is shown in Additional file 1: Table S1.

·OH scavenging capacity of CNs

To determine the ·OH scavenging capacity of CNs, an ·OH scavenging capacity assay kit was used. According to the operation instructions, the [Fe(phen)₃]²⁺/H₂O₂ system generated ·OH, and the scavenging capacity of the CNs for ·OH was reflected by the degree of the absorbance decline rate at 536 nm. The absorbance (OD values) at 536 nm was measured by an enzyme-labeled instrument, the calculation formula is ·OH scavenging rate (%) = $(A_{\text{sample}} - A_{\text{control}}) / (A_{\text{blank}} - A_{\text{control}}) \times 100\%$.

SOD-like catalytic activity

The SOD-like catalytic activity of CNs was tested using a SOD assay kit according to the protocol. The working

solution was added to CNs with different concentrations (50, 100, 200, 400, 800, and 1600 $\mu\text{g}/\text{mL}$, protein concentration), and followed by thorough mixing and water bath at 37 °C for 40 min. Then the absorbance value was measured at 550 nm using UV–Vis (UV1800PC, Jinghua Co., Ltd. Shanghai, China) after adding chromophore and standing at room temperature for 10 min. Meanwhile, the color changes of different samples were recorded by the camera. The SOD-like activity of the sample was expressed by the inhibition ratio relative to the blank control.

Catalase (CAT)-like catalytic activity

The H_2O_2 scavenging effect of the CNs was detected using a hydrogen peroxide detection kit. All samples were incubated with H_2O_2 (50 mM) at room temperature, and the concentration of the remaining H_2O_2 was calculated at different time intervals (10 and 60 min) following the provided protocol.

Oxygen (O_2) generation was observed in a 1 mL test tube. Disperse 200 μL different concentrations of CNs to 800 μL 10 mM H_2O_2 solution to observe the amounts of bubbles after 1, 5, and 10 min. The generated O_2 was recorded by a digital camera and quantitatively tested with a dissolved oxygen meter (JPB-607A, Leici).

The total antioxidant activity of the CNs

The total antioxidant activity of the CNs was investigated by ABTS^+ assay. According to the protocols, samples of different concentrations were mixed with pre-prepared ABTS^+ working solution for 6 min at room temperature. After that, the resultant mixture was detected by UV–Vis absorbance spectroscopy. Meanwhile, pictures were taken to record the change of the colors after the reaction. The formula is the free radical scavenging rate (%) = $(A_{\text{blank}} - A_{\text{sample}}) / A_{\text{blank}} \times 100$.

Cell uptake and internalization mechanism of CNs in vitro

CNs were labeled with the fluorescent dye DiO (D-CNs). Briefly, D-CNs were prepared by mixing 1 mg/mL of DiO dye with a 4 mg/mL CNs solution at a volume ratio of 1:5, followed by incubation at 37 °C for 30 min. The suspension was then purified using dialysis to remove any free DiO dye. The amount of labeled fluorescent dye was quantified using a fluorescent microplate reader (MD SpectraMax M5, USA, Ex: 484 nm, Em: 501 nm).

For cellular uptake studies, MC3T3-E1 cells were seeded in 6-well plates (5×10^5 cells per well) with 2 mL of DMEM to study the cellular uptake efficiency of CNs. After treatment with 200 $\mu\text{g}/\text{mL}$ D-CNs and equal fluorescent concentrations of single DiO dye, the cells were collected at predesigned time points (0, 2, 4, 8 h) and analyzed with confocal laser scanning microscopy

(CLSM, Leica SP8, Germany) and flow cytometer (Beckman Coulter, USA).

To study the mechanism of CNs internalization, after being seeded in 6-well plates for 24 h, MC3T3-E1 cells were pretreated with different endocytosis inhibitors including 28 μM chlorpromazine (clathrin endocytosis inhibitor), 100 μM β -cyclodextrin (caveolin endocytosis inhibitor), 0.01 μM cytochalasin D (actin-dependent endocytosis inhibitors) and 10 μM amiloride (giant pinocytosis specific inhibitor) for 30 min, and D-CNs (200 $\mu\text{g}/\text{mL}$) were added to different groups for additional 4 h of incubation. Cells were collected and analyzed using flow cytometry.

Cell cultures and construction of oxidative stress cell model

MC3T3-E1 cells were cultured at 37 °C and 5% CO_2 atmosphere in a DMEM culture medium containing 10% FBS and 1% P/S antibiotic solution. After reaching confluence, the cells were treated with the FBS-free medium containing different concentrations of H_2O_2 (0.25, 0.5, 0.75, 1 mM) for 3 h, 6 h, and 24 h. According to the cell survival rate, 1 mM was finally selected as the model concentration.

Intracellular ROS determination

The level of intracellular ROS was tested using the fluorescent probe DCFH-DA in the ROS detection kit. MC3T3-E1 cells in 6-well culture plates were incubated with 200 $\mu\text{g}/\text{mL}$ CNs for 24 h before treatment with 1 mM H_2O_2 for 6 h. Then, the cells were washed with PBS twice, and serum-free culture medium was incubated with 2 μM DCFH-DA at 37 °C for 30 min. The cells were washed with PBS twice to eliminate the unlabeled DCFH-DA. The relative levels of fluorescence intensity were characterized by flow cytometry and CLSM.

Alkaline phosphatase staining and alizarin red S staining

For the alkaline phosphatase expression assay, cells were cultured in 6-well plates at a density of 1×10^5 cells per well. After incubation with DMEM medium containing different concentrations of CNs (50, 100, 200, and 400 $\mu\text{g}/\text{mL}$) for 24 h, the H_2O_2 group and H_2O_2 +CNs group were treated with 1 mM H_2O_2 for 6 h. After 3 days, cells were fixed using paraformaldehyde (4%) and stained with a BCIP/NBT alkaline phosphatase color development kit. We performed the staining following the manufacturer's protocol and images were captured using a DM500 microscope (Leica, Germany) and semi-quantified via ImageJ software.

To study the mineralization level, MC3T3-E1 cells were seeded into 6-well plates at the density of 1×10^5 cells per well and cultured in DMEM supplemented with varying concentrations of CNs (50, 100, 200, and 400 $\mu\text{g}/\text{mL}$) and

stimulated with H₂O₂ to assess mineralization. After 5 days, then the cells were fixed with a 4% paraformaldehyde solution, washed with PBS, and stained with ARS solution. Images were recorded by a DM500 microscope and semi-quantified via ImageJ software.

Assessment of mitochondrial function

Mitochondrial membrane potential was assessed using the dye 5, 5', 6, 6'-Tetrachloro-1, 1', 3, 3'-tetraethylimidacarbocyanine iodide (JC-1) and visualized using a fluorescence microscope (Leica, Germany). MC3T3-E1 cells were seeded at the density of 3×10^5 cells per well in 6-well plates and allowed to adhere overnight. After all of the treatments, the cells were stained with a working solution prepared by JC-1 stain (100 \times) for 20 min at 37 °C. After incubation, the supernatant was removed and washed twice with PBS. Fluorescence images were scanned using a fluorescence microscope, and the fluorescence intensity was quantified with ImageJ software. The protocol involves opening the image, extracting a single channel, adjusting the threshold, selecting the appropriate region, and then checking the 'dark background' option to measure the mean gray value. The ratio of red and green fluorescence was counted and normalized.

For observing the morphology of mitochondria, MC3T3-E1 cells were seeded at the density of 1×10^6 cells/well in a 6-well culture plate and cultured overnight. After all of the treatments, Bio-TEM was performed according to the following procedure. Cells were fixed with 2.5% glutaraldehyde for 12 h. After being dehydrated and dried, cells were cut into ultrathin sections (70–90 nm). After being stained with uranyl acetate and lead citrate for 10 min, sections were dried and performed using a TEM microscope (Hitachi, HT7800).

Functional Mitochondrial morphology was evaluated using the MitoTracker Red CMXRos dye according to the manufacturer's instructions. Briefly, MC3T3-E1 cells were seeded in confocal dishes at a density of 1×10^5 cells per well and treated with 200 μ g/mL CNs for 24 h before being stimulated with 1 mM H₂O₂ for 6 h. The cells were then incubated in a serum-free medium containing 200 nM of the probe in the dark at 37 °C for 20 min. The cells were subsequently washed twice in PBS and the nuclei were stained with Hoechst 33342 at 10 μ g/mL for 20 min. Images were acquired with CLSM.

MC3T3-E1 cells were seeded in XF24 cell culture microplates (Agilent). Cellular oxygen consumption was measured with a Seahorse XFe24 Analyzer (Agilent). When the confluence of cells reached about 50%, the cells were treated with 200 μ g/mL CNs or DMEM medium for 24 h and then stimulated with H₂O₂ for 6 h. After the basal readings, 1.5 mM oligomycin, 1 mM Carbonyl Cyanide 4-(Trifluoromethoxy) phenylhydrazone (FCCP) and

0.5 mM rotenone/antimycin A were injected in sequence. Data were collected and analyzed using Seahorse Wave Desktop software. The data normalization of oxygen consumption measurements was performed using the cell number at the end of the experiments, and mitochondrial respiration was expressed as oxygen consumption rate (OCR, pmol/min/cells).

Apoptosis assay

The apoptosis of MC3T3-E1 cells was tested using the Annexin V-FITC apoptosis detection kit. Different treated cell suspensions were collected according to the method provided in the instructions. Cell suspensions (1×10^6 cells /mL) were incubated with 5 μ L Annexin V-FITC and 10 μ L Propidium Iodide (PI) staining solution. After incubation for 15 min at room temperature in the dark, 400 μ L $1 \times$ Annexin V binding buffer was added to the cell suspensions. Then cells were analyzed using a flow cytometer and data were analyzed using FlowJo software.

TUNEL assay was performed according to the protocol to detect cell apoptosis. After different treatments, the medium was removed and the cells were fixed with 50 μ L 4% paraformaldehyde for 30 min at room temperature. The fixative was removed and washed three times with PBS for 5 min per well. Afterward, each well was added 0.3% Triton X-100 and incubated for 30 min at room temperature. Finally, after the transparent agent was removed, cells were washed with bovine serum albumin (BSA) working solution 3 times and imaged under fluorescence microscopy.

The determination of Caspase-3 activity was detected by the Caspase-3 activity analysis kit (colorimetric method). After all of the treatments, cells were collected and resuspended in a working cell lysis buffer. The lysate was incubated for 15 min on ice, and centrifuged on $15,000 \times g$ at 4 °C for 15 min. Enzyme activity was measured according to the manufacturer's instructions. In simple terms, samples and working liquid were mixed and incubated at 37 °C for one hour, enzyme standard instrument was used to detect 405 nm absorbance values.

Transcriptome sequencing

RNA sequencing was used to detect differential gene expression in the control, H₂O₂, and H₂O₂ + CNs groups. MC3T3-E1 cells in the culture dish were incubated with DMEM medium containing 200 μ g/mL CNs for 24 h before treatment with 1 mM H₂O₂ for 6 h. Total RNA was extracted from the MC3T3-E1 cells using Trizol reagent according to the manufacturer's instructions (Invitrogen, USA). After washing twice with PBS, 1 mL of Trizol reagent was added to a precipitate of 5×10^6 cells, and the cells were repeatedly whipped until no cell clumps

remained. RNA samples were assessed based on the A260/A280 absorbance ratio with a Nanodrop ND-2000 system (Thermo Scientific, USA), and the RIN of the RNA was determined by an Agilent Bioanalyzer 4150 system (Agilent Technologies, CA, USA). Three replicate samples were taken from each group and detailed data for each sample are shown in Additional file 1: Table S2. Transcriptome sequencing was performed with an Illumina NovaSeq 6000/MGISEQ-T7 instrument and the data were analyzed using the Illumina/BGI platform. Differentially expressed genes (DEGs) analysis was conducted using the DESeq2 (<http://bioconductor.org/packages/release/bioc/html/DESeq2.html>). Gene expression changes with fold change > 2 and p-value < 0.05 were considered significant. KEGG pathway enrichment and GO function enrichment analysis were utilized by using the clusterProfiler R software package. When p < 0.05, it is considered that the GO or KEGG function is significantly enriched. Finally, the results were visualized through the Bio-cloud platform (<https://bio-cloud.apptbiotech.com/project>).

Measurement of intracellular calcium concentration

According to the manufacturer's instructions, a calcium colorimetric assay kit was used to measure calcium concentration. Briefly, the MC3T3-E1 cells were cultivated in a 6-well plate and treated with 200 µg/mL CNs under conditions of H₂O₂ stimulation, then washed with PBS and lysed with lysis buffer. After centrifugation, the cell lysate solution was collected and mixed with the working color solution. The mixtures were then incubated at room temperature for 10 min to detect the absorbance at 575 nm using a microplate reader. To normalize the amount of calcium, protein concentrations were measured using a BCA protein assay kit.

qPCR analysis

For qPCR analysis, MC3T3-E1 cells were cultured in different treatment groups. The control group was cultured using DMEM medium, the H₂O₂ group was treated only with H₂O₂ for 6 h, and the H₂O₂ + CNs group was treated with 200 µg/mL CNs followed by H₂O₂ stimulation for 6 h. Total RNA was collected using an M5 Hiper Universal Plus RNA Mini Kit. Subsequently, cDNA was synthesized using a cDNA transcription kit. Amplification reactions were performed using 3 µL of cDNA template, 0.5 µL of primer, 6 µL of distilled deionized water, and 10 µL of SYBR Green in a StepOne Plus PCR machine for 50 cycles. The sequences of the primers used are provided in Additional file 1: Table S3. The starting quantities of the samples were determined using the 2^{-ΔΔT} methods and normalized to the internal reference gene GAPDH. The

data presented for each group represent the fold-change in relative mRNA expression levels of target genes, normalized to the control group.

Pharmacokinetic profile

All animal experiments were approved by the Ethics Committee Second Hospital of Shanxi Medical University with the approval number (DW2023040). To study the pharmacokinetic profile, C57BL/6J mice (about 8 weeks old) were purchased from SPF Experimental Animal Company (Beijing, China). The mice were administered with D-CNs (1 mg/mL) via tail vein injection. At given times (0.25, 0.5, 2, 4, 8, 12, 24 h), the blood was collected from the mouse eyes and centrifuged at 3000 × g at 4 °C for 10 min to obtain the supernatant plasma. The content of D-CNs was measured by a fluorescent microplate reader. Pharmacokinetic software (DAS 3.0) was used to analyze data.

In vivo imaging and biodistribution

Three groups of ovariectomized (OVX) mice (n = 3) were treated with PBS, DiR, and DiR-loaded CNs (DiR-CNs). CNs were labeled with DiR as provided by the manufacturer, 100 µL of DiR dye working solution was added to 1 mL of the CNs suspension and vortexed to mix, then incubated at 37 °C for 30 min, and unlabeled dye was removed by dialysis to obtain DiR-CNs. After injection for 24 h, the mice were anesthetized and the whole body fluorescence signals (Ex: 747 nm, Em: 780 nm) were recorded using a small animal in vivo fluorescence imaging system (PerkinElmer IVIS Lumina LT III, USA). The major organs, including the heart, liver, spleen, lungs, kidney, femur, and tibia tissues, were carefully excised to detect the distribution of CNs using living image analysis software (Caliper Life Sciences, Inc., USA).

OVX-induced osteoporotic mouse model and osteoporosis treatment in vivo

8-week-old female C57BL/6J mice underwent bilateral ovariectomy to induce osteoporosis. Both ovaries were carefully removed, ensuring that no ovarian tissue remained. The mice were housed in a specific pathogen-free (SPF) environment and referred to as OVX mice. Mice in which only adipose tissue adjacent to the ovary was removed served as the sham group. One week after the surgery, once their wounds had healed, the mice were divided into four groups, each consisting of five mice. The experimental groups were as follows: a sham-operated group (Sham), which received PBS treatment via tail vein injection every 3 days; a model group consisting of ovariectomized (OVX) mice treated with PBS via tail vein injection every 3 days; OVX mice treated with CNs at a dose of 2.5 mg/kg via tail vein injection every 3 days

(OVX + CNs); and OVX mice treated with 17β -estradiol (E_2) at a dose of 0.5 mg/kg via tail vein injection every 3 days (OVX + E_2). After the whole treatment period, mice were sacrificed after 8 weeks. The femurs were collected and fixed in 4% neutral paraformaldehyde for 24 h. Tissues were scanned and analyzed with micro-computed tomography (Micro-CT, Bruker microCT, Kontich, Belgium) using the following scanning conditions: source voltage 55 kV; source current 200 μ A; Al 0.25 mm filter; pixel size 6 μ m; rotation step 0.3 degree. The images were then reconstructed with NRecon software (Bruker microCT, Kontich, Belgium) using the following settings: ring artefactor rection, 5; smoothing, 3; beam hardening correction, 30%. Bone volume fraction (BV/TV), trabecular thickness (Tb. Th), trabecular number (Tb. N), trabecular spacing (Tb. Sp), and bone mineral density (BMD) were analyzed by the program CTAN (Bruker microCT, Kontich, Belgium). BV/TV represents the ratio of bone volume to total tissue volume, providing a direct measure of changes in bone mass. BMD reflects the mineral content within the bone tissue of the selected region. Tb. N indicates the average number of intersections between bone and non-bone tissue per millimeter within the region of interest. Tb. Th represents the average thickness of the trabecular bone. Tb. Sp refers to the average distance between the bone trabeculae, representing the width of the medullary cavity.

The femurs and tissue were collected, fixed in 4% paraformaldehyde, and transferred to 10% ethylene diamine tetraacetic acid (EDTA) solution for decalcification for 4 weeks. They were sequentially dehydrated, embedded in paraffin, sectioned (5 μ m thick), and subjected to H&E staining and Masson staining.

For immunohistochemistry analysis, block the sections first for 0.5 h with 5% BSA at room temperature and then incubate them overnight at 4 °C with the corresponding primary antibodies: JNK and Dusp10. Subsequently, the slices were incubated with the corresponding secondary antibody at 37 °C for 30 min and then treated with DAB chromogenic solution for 15 min. For immunofluorescence analysis, put the slices neatly on a wet box, draw a circle around the tissue with a histochemical pen circle,

add the prepared DHE antibody diluent, and then place the wet box in an oven at 37 °C for 30 min, wash with PBS three times, and then seal the slides using an anti-fluorescence quenching sealer. Finally, image acquisition of the sections was performed using a micro camera system (BA400Digital), and the positive area analyses were performed by ImageJ software.

In vivo safety evaluation

After completing the entire treatment period, the mice were euthanized. The serum samples were collected to measure the levels of alanine transaminase (ALT), aspartate aminotransferase (AST), blood urea nitrogen (BUN), creatinine (CREA), inorganic ionic calcium (Ca), and phosphorus (P). The whole blood sample was collected for a routine blood test. Tissues including heart, liver, spleen, lung, and kidney were used for H&E staining.

Statistical analysis

Data were assessed for homogeneity of variances using Levene's test before statistical analysis in SPSS 26.0. For multiple comparisons, a one-way analysis of variance (ANOVA) was performed, followed by the Tukey post-hoc test when variances were homogeneous and the Tamhane post-hoc test when variances were unequal. For two-group comparisons, a two-tailed Student's *t*-test was conducted using GraphPad Prism 9.5 software. This approach applies to both in vitro and in vivo data, except for transcriptome sequencing, for which statistical methods are detailed in the corresponding legend. All data were presented as mean \pm standard deviation (s.d.), with **p* < 0.05, ***p* < 0.01, and ****p* < 0.001 considered statistically significant, and NS indicating no significance.

Results and discussion

Isolation and characterization of carrot-derived nanoantioxidants

First, nanovesicles were obtained from carrot juice through a simple extrusion approach [54]. Based on TEM examination (Fig. 1A, Additional file 1: Fig. S1), CNs had round structures and characteristic lipid bilayers. As displayed in Fig. 1B, CNs had an average size of 137.8 nm,

(See figure on next page.)

Fig. 1 Characterization and ROS scavenging effectiveness of the CNs. **A** TEM showing the morphological features of CNs. Scar bar: 100 nm. **B** Size distribution and **C** zeta potential of CNs. **D** The particle size and concentration of CNs were analyzed by NTA. **E** Stability of CNs under different pH conditions by measuring the size change at different times (*n* = 3). **F** Subcellular localization of CNs proteins. **G** Pie chart of the proportion of the content of identified superclass metabolites of CNs in each chemical category. **H** Distribution of subclass metabolites of the top three superclass metabolites in content. **I** Schematic illustration of antioxidative activities of CNs. **J** ·OH scavenging rate of different concentration CNs (*n* = 3). **K** UV–Vis absorption spectra showed SOD-like activity of CNs at different concentrations. **L** The decomposition of H₂O₂ (50 mM) reacted with various concentrations of CNs was detected at 10 and 60 min (*n* = 3). **M** O₂ generated in H₂O₂ (2 mM) solution of CNs in 1 min was detected by the dissolved oxygen measurement instrument. **N** UV–Vis absorption spectra showed the total antioxidation activity of CNs at different concentrations by the ABTS⁺ assay. All data were presented as mean \pm s.d.

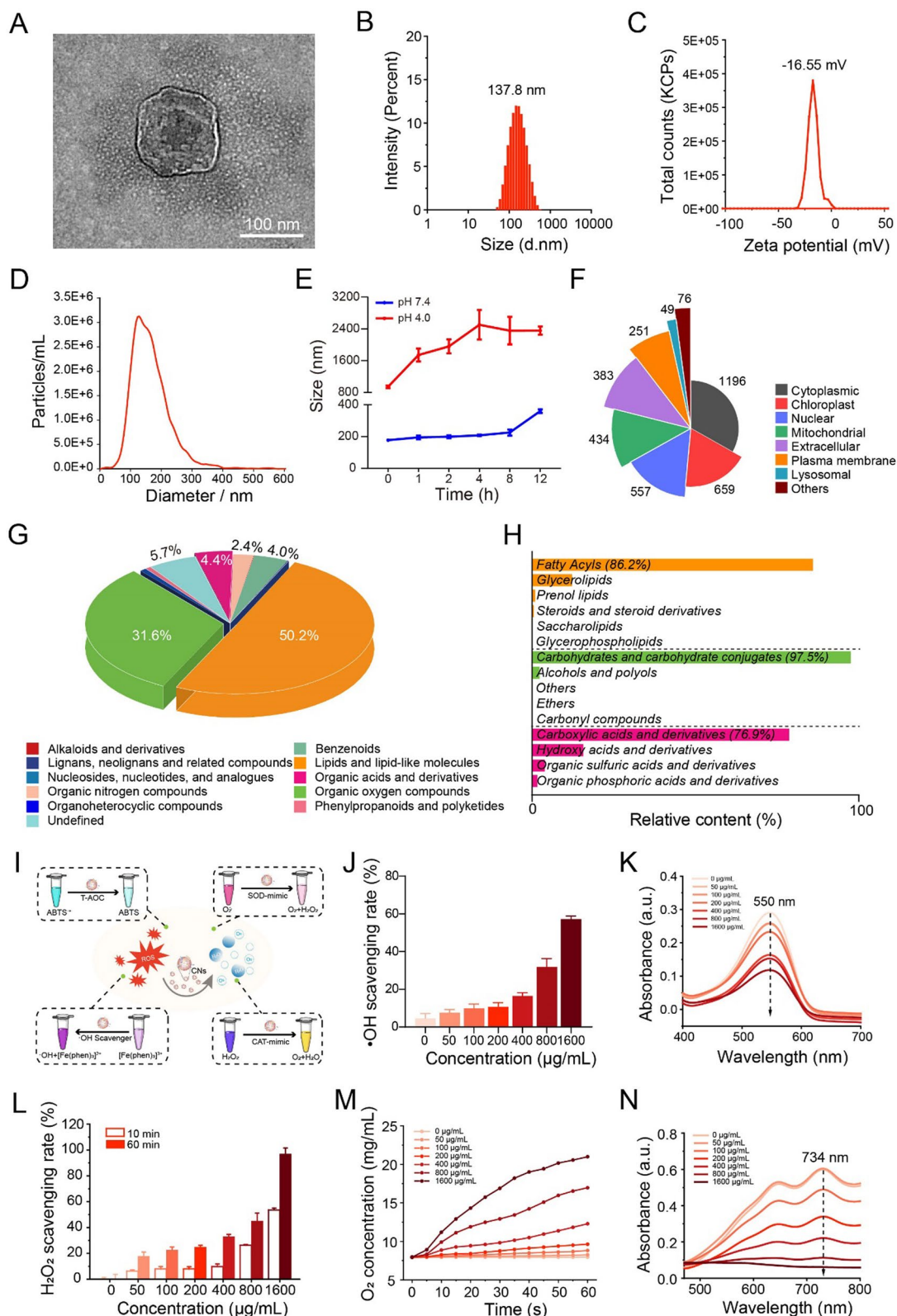


Fig. 1 (See legend on previous page.)

which well agreed with the TEM result. These CNs had a zeta potential of -16.5 mV (Fig. 1C). Meanwhile, NTA analysis determined a particle size of 128.7 nm and a particle concentration of 5.5×10^9 particles/mL (Fig. 1D). Besides, these nanovesicles had steady nanostructures under normal physiological conditions (pH 7.4). However, upon exposure to acidic conditions mimicking the osteoporotic microenvironment (pH 4.0), CNs undergo a transformation into larger particles. This change occurs due to alterations in surface charge (from -16.5 mV to -6.9 mV) driven by electrostatic interactions, which may potentially enhance their retention within bone tissue (Fig. 1E, Additional file 1: Fig. S2). It was noted that different batches of CNs had consistent protein concentrations (~ 4.5 mg/mL, Additional file 1: Fig. S3). In addition, CNs stored at different temperatures (4, -20 , and -80 °C) for 2 weeks maintained stable nanostructures, surface charges, and protein content (Additional file 1: Fig. S4-S6). Carrot-derived exosomes were isolated using density gradient ultracentrifugation [36, 55]. Compared to CEs, CNs exhibited approximately a 113.2-fold increase in protein concentration. (Additional file 1: Fig. S7A-S7C). The SDS-PAGE analysis revealed that the proteins from CNs were primarily distributed within the molecular weight range of 10–100 kDa (Additional file 1: Fig. S8). We made use of proteomic analysis to study the protein components in detail. A total of 2684 proteins were identified and quantified in the CNs. Subcellular distribution predictions classified these proteins as follows: 1,196 cytoplasmic proteins, 659 chloroplast proteins, 557 nuclear proteins, 434 mitochondrial proteins, 383 extracellular proteins, 251 plasma membrane proteins, and 49 lysosomal proteins (Fig. 1F). The KEGG enrichment analysis revealed that the most enriched pathways were associated with ribosome function and glycolysis (Additional file 1: Fig. S9). The GO enrichment analysis indicated that the predominant enriched molecular functions were catalytic activity and antioxidant activity (Additional file 1: Fig. S10) [56, 57]. A non-targeted metabolomics analysis was conducted to examine the metabolite composition of CNs, identifying a total of 286 metabolites, which were categorized into 11 superclasses. (Additional file 1: Fig. S11). As shown in Fig. 1G of the quantitative proportions of metabolites, lipids (50.2%) and organic oxygen compounds (31.6%) were enriched in CNs, where fatty acyls (86.2% of total lipids), and carbohydrates (97.5% of total organic oxygen compounds) were detected, respectively (Fig. 1H, Additional file 1: Fig. S12). Therefore, nanovesicles derived from carrots were successfully extracted with stable membrane structures and multiple active ingredients for potential biological application.

Recent studies have shown that excessive generation of ROS leads to decreased osteoblast activity and

even apoptosis [14, 58] (Fig. 1I). First, we tested the $\cdot\text{OH}$ scavenging capacity of CNs through the Fenton reaction. As displayed in Fig. 1J, the $\cdot\text{OH}$ scavenging rate of CNs increased significantly, reaching up to 57.2% as the concentration increased to 1600 $\mu\text{g/mL}$, demonstrating a great $\cdot\text{OH}$ eliminating capacity. SOD, an intracellular enzyme, plays a pivotal role in the antioxidant process by converting $\text{O}_2^{\cdot-}$ into H_2O_2 and O_2 . Hence, the SOD-like activity of CNs was measured using a T-SOD assay kit based on the hydroxylamine method. Optical images showed that the purplish-red color gradually disappeared with the increase in CNs concentration (Additional file 1: Fig. S13). UV-Vis spectra results indicated that the absorbance value at 550 nm weakened from 0.29 to 0.12 a.u. after treatment with various concentrations of CNs, which was ascribed to the strong $\text{O}_2^{\cdot-}$ scavenging ability mimicking SOD enzyme (Fig. 1K, Additional file 1: Fig. S14). Subsequently, we determined the CAT-like capacity which could decompose H_2O_2 into H_2O and O_2 . As shown in Fig. 1L, CNs demonstrated significant scavenging efficiency on H_2O_2 . At a concentration of 1600 $\mu\text{g/mL}$, approximately 96.9% of H_2O_2 was eliminated after 60 min. It was observed that a greater number of bubbles were produced in the test tube treated with CNs compared to the untreated control group (Additional file 1: Fig. S15). After incubation with 1600 $\mu\text{g/mL}$ CNs, the generation of O_2 fleetly reached 21.0 mg/mL in the 60 s (Fig. 1M), indicating a strong CAT-mimic activity. To further study their antioxidant performance, the total ROS-eliminating ability was tested using the ABTS^+ radical assay. The characteristic absorption peaks of ABTS^+ at 734 nm significantly decreased after treatment with various concentrations of CNs (Fig. 1N, Additional file 1: Fig. S16-S18). Furthermore, CNs exhibited a stronger antioxidant capacity compared to CEs (Additional file 1: Fig. S7D). In summary, the results above demonstrated that CNs displayed a variety of enzyme-mimic activities and possessed exceptional antioxidant capacities.

CNs restore osteoblast activity in the osteoporotic microenvironment

Once the ROS-eliminating activity was confirmed, we turned to investigate whether CNs could induce osteoblast proliferation and facilitate osteogenesis in vitro. As shown in Fig. 2A, CNs could distinctly promote MC3T3-E1 cell proliferation at various concentrations ranging from 0 to 400 $\mu\text{g/mL}$. Particularly, the cell viability increased to 3.3 times after treatment with 400 $\mu\text{g/mL}$ CNs from day 1 to day 5. To further investigate cellular uptake efficiency, CNs were labeled with DiO, a commercial fluorescent dye known for its strong membrane affinity. CLSM images showed that the DiO-labeled CNs primarily adhered to the cell membrane during the first

1 to 4 h, and were internalized into the cytoplasm after 8 h of exposure (Fig. 2B). Flow cytometry quantitative results demonstrated that D-CNs provided strong cellular uptake efficiency with 99.6% positive cells after incubation for 8 h (Fig. 2C, D). However, free DiO dye exhibited higher cellular uptake efficiency compared to D-CNs. This difference may be attributed to the membrane-affinity properties of DiO, which allows it to bind to the cell membrane more rapidly than D-CNs (Additional file 1: Fig. S19, S20). To disclose the mechanism of internalization, endocytosis pathways of MC3T3-E1 cells were blocked using various inhibitors. As shown in Fig. 2E and F, the positive cell decreased to 54.3% after exposure to chlorpromazine (clathrin endocytosis inhibitor). However, there was no influence on the internalization of D-CNs in the presence of β -cyclodextrin (caveolin endocytosis inhibitor), amiloride (giant pinocytosis specific inhibitor), and cytochalasin D (actin-dependent endocytosis inhibitors) [59, 60]. Hence, the cellular uptake of CNs mainly relied on the clathrin endocytosis pathway. Then, MC3T3-E1 cells were treated with H₂O₂ to induce oxidative stress, simulating the detrimental microenvironment characteristic of osteoporosis. Cell viability decreased in a concentration-dependent and time-dependent manner. The survival rate of cells stimulated with 1 mM H₂O₂ for 6 h was 53.1%, which was used for subsequent studies (Additional file 1: Fig. S21–S23). After treatment with 200 and 400 μ g/mL CNs for 24 h, cell viability was raised to 78.5% and 82.8% respectively, manifesting that CNs competently protected the cells from ROS destruction (Fig. 2G). ROS levels in MC3T3-E1 cells were seriously elevated after pretreatment with 1 mM H₂O₂ compared to the control group assessed using a DCFH-DA fluorescent detector. However, after the cells were treated with CNs, there was a noticeable decrease in green fluorescence signals and a reduction in the number of positively stained cells (13.9%), indicating

the strong ROS-eliminating capacity in vitro (Fig. 2H). Next, we turned to access the osteogenic differentiation abilities in the osteoporotic microenvironment (Additional file 1: Fig. S24–S27). ALP staining images demonstrated that CNs effectively rescued MC3T3-E1 cells from a high oxidative stress environment and reprogrammed osteoblasts with the highest ALP expression observed at concentrations above 200 μ g/mL (Fig. 2I, J). In addition, the calcium mineral deposition stained with Alizarin red S was lower in the H₂O₂ pretreatment group compared to the control group. However, there was a significantly higher amount of calcium mineral deposition observed after incubation with 200 μ g/mL CNs. Moreover, this value increased 8.2-fold over time, suggesting that CNs can reprogram osteoblasts into osteogenic differentiated cells even under conditions of intense oxidative stress (Fig. 2I, K). Furthermore, the mRNA levels of osteogenic markers, including alkaline phosphatase (ALP), runt-related transcription factor 2 (Runx2), osteopontin (OPN), and osteocalcin (OCN), were up-regulated by 1.58, 1.72, 2.12, and 1.42 times in the H₂O₂ + CNs group respectively, which efficiently counteracted the oxidative stress effect of H₂O₂ (Fig. 2L–O)[61]. In consequence, CNs demonstrated potential as nanoantioxidants that could significantly reduce ROS generation and alleviate oxidative stress, thereby promoting osteogenic differentiation in the osteoporotic microenvironment.

Since mitochondria are closely associated with oxidative stress and apoptosis, we next investigated their impact on cellular biological functions. First of all, the mitochondrial membrane potential ($\Delta\Psi_m$) of MC3T3-E1 cells, a critical indicator of mitochondrial function, was evaluated using the cationic dye JC-1, which could form aggregates (red fluorescence) in mitochondria with high $\Delta\Psi_m$ levels but shift to a monomer (green fluorescence) in the cytosol when the mitochondria were damaged. As shown in CLSM images and quantitative results,

(See figure on next page.)

Fig. 2 CNs reduce oxidative stress and promote osteogenic differentiation. **A** Cell viability of MC3T3-E1 cells treated with different concentrations of CNs over 5 days (n = 3). **B** CLSM images for observing cellular uptake of D-CNs at different times. Blue fluorescence represents cell nuclei stained by Hoechst 33342, green fluorescence represents DiO-labeled CNs. Scar bar: 30 μ m. **C** Flow cytometry images and **D** mean fluorescence intensity of D-CNs at different times for detecting cellular uptake (n = 3). **E** Flow cytometry images and **F** quantitative analysis of the D-CNs internalization after pretreatment with different inhibitors (n = 3). ****p* < 0.001. Statistical significance was calculated by one-way ANOVA, followed by the Tukey post-hoc test. **G** Cell viability of MC3T3-E1 cells vs different concentrations of CNs under the condition of oxidative stress, 1 mM H₂O₂ stimulates cells 6 h to build an oxidative stress model (n = 3). ***p* < 0.01, ****p* < 0.001. Statistical significance was calculated by one-way ANOVA, followed by the Tukey post-hoc test. **H** Flow cytometry images and CLSM images of intracellular ROS in MC3T3-E1 under different treatment conditions stained by DCFH-DA. Scar bar: 100 μ m. **I** ALP and ARS staining images of MC3T3-E1 cells after incubation with different concentration CNs under H₂O₂ stimulation. **J** Semi-quantitative statistics of ALP expression positive area of MC3T3-E1 cells on day 3 after treatment with CNs under conditions of oxidative stress (n = 3). ****p* < 0.001. Statistical significance was calculated by one-way ANOVA, followed by the Tamhane post-hoc test. **K** Semi-quantitative of mineralized nodules of MC3T3-E1 cells on day 5 after treatment with CNs under conditions of oxidative stress (n = 3). ****p* < 0.001. Statistical significance was calculated by one-way ANOVA, followed by the Tamhane post-hoc test. **L–O** qPCR analysis for mRNA levels of osteogenic markers including ALP (**L**), Runx2 (**M**), OPN (**N**), and OCN (**O**), n = 3. **p* < 0.05, ***p* < 0.01, ****p* < 0.001. Statistical significance was calculated by one-way ANOVA, followed by the Tukey post-hoc test). All data were presented as mean \pm s.d.

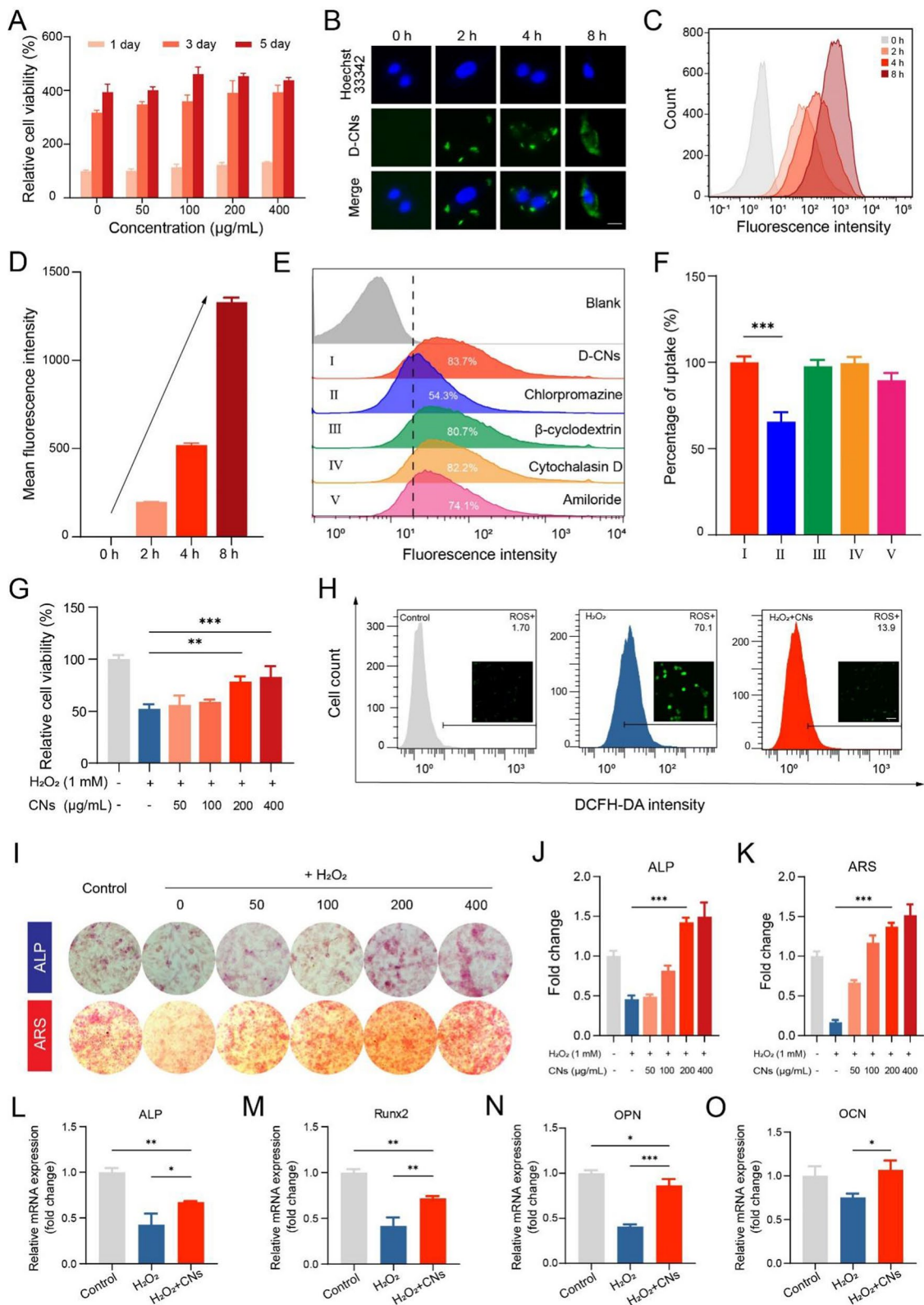


Fig. 2 (See legend on previous page.)

the red/green ratio declined to 52.7% in the H₂O₂ group compared to the control group, testifying serious mitochondrial damage and cell apoptosis. Nevertheless, there was a significant increase in the red/green ratio (85.8%) after exposure to 200 µg/mL CNs for 24 h, implying an apparent protection against oxidative stress (Fig. 3A, C, Additional file 1: Fig. S28-S30). Bio-TEM images showed that mitochondrial membrane density increased and mitochondrial cristae decreased or even vanished upon H₂O₂ stimulation, which was significantly restored after CNs treatment (Fig. 3B, D). We turned to visualize the dynamic changes of the mitochondria by confocal microscopy after MitoTracker staining. As shown in Fig. 3E, the mitochondria in the H₂O₂ group exhibited shrinkage and a reduced area. However, treatment with CNs significantly restored the mitochondrial morphology, suggesting a recovery of mitochondrial integrity and function. Next, we assessed mitochondrial functionality by measuring the oxygen consumption rate (pmol/min/cells) using Seahorse technology. After treatment with 1 mM H₂O₂, basal respiration, mitochondrial-linked ATP production, and maximal respiration, were significantly reduced compared to the control group. The addition of 200 µg/mL CNs enhanced basal respiration, maximal respiration, and mitochondrial-linked ATP production, indicating that CNs could effectively restore mitochondrial functionality (Fig. 3F, G). Meanwhile, the activity of pro-apoptotic Caspase-3 was raised 5.1-fold once pretreatment with 1 mM H₂O₂ compared to the control group. As expected, the treatment of 200 µg/mL CNs dramatically down-regulated the activity of Caspase-3 (Fig. 3H). Since excess ROS plays a critical role in apoptosis, TUNEL staining images revealed that oxidative stress induced by H₂O₂ significantly triggered apoptosis in MC3T3-E1 cells. In contrast, the CNs group exhibited minimal apoptosis, as indicated by a weak red fluorescence signal (Fig. 3I). Besides, we used flow cytometry to investigate the fate of MC3T3-E1 cells

following treatment with CNs. Pretreatment with H₂O₂ resulted in 7.2% late apoptotic cells and 4.5% necrotic cells. However, CNs significantly protected MC3T3-E1 cells from apoptosis, resulting in a low proportion of apoptotic (5.0%) and necrotic (2.7%) cells (Fig. 3J, K). The qPCR results also demonstrated that H₂O₂ increased the mRNA levels of the pro-apoptotic gene BCL2-associated X (Bax) and inhibited the expression of the anti-apoptotic gene B-cell lymphoma-2 (Bcl-2) compared to the control group (Fig. 3L). Taken together, CNs could successfully protect osteoblast cells from apoptosis thanks to their powerful antioxidant capacity.

To explore the combined effects of lipid and organic oxygen compounds derived from CNs, large unilamellar vesicles as mimicking CNs (MCNs) composed of GMS, Eru, Fru, and QA were prepared using the membrane-sonication method (Fig. 4A) [62]. The concentrations of GMS, Eru, Fru, and QA in MCNs align with the contents observed in CNs (Additional file 1: Table S1). As shown by the DLS results in Fig. 4B and C, MCNs had an average size of 267.2 nm and a negative surface charge of -22.8 mV, similar to the nanostructures of CNs. Next, we proceeded to test the total ROS elimination ability using the ABTS⁺ assay. Single compounds, such as GMS, Eru, Fru, and QA, exhibited a very weak antioxidant capacity, as they were able to eliminate less than 10% of ABTS⁺ radicals. When these compounds were prepared into MCNs, the clearance rate was significantly increased to 13.0%. As anticipated, our CNs exhibited the highest clearance rate of 70.1%, illustrating the synergistic effect of many kinds of compounds (Fig. 4D). In addition, we also disclose their biocompatibility with MC3T3-E1 cells under high oxidative stress that mimics the microenvironment of osteoporosis (Fig. 4E). Individual GMS and Eru molecules exhibited significant cytotoxicity towards MC3T3-E1 cells over a 24-h treatment period, which may be attributed to their hydrophobic nature and their ability to disrupt cell membranes. However, both MCNs and

(See figure on next page.)

Fig. 3 CNs improve osteoblast function in the osteoporotic microenvironment. **A** Representative fluorescent images under different treatment conditions detected by JC-1 staining (n=3). Scar bar: 200 µm. **B** Representative images of mitochondrial morphology under Bio-TEM (n=3). Scar bar (from top to bottom): 2 µm, 1 µm, 20 nm. **C** Semi-quantitative analysis of ΔΨ_m under different treatment conditions detected by JC-1 staining (n=3. **p<0.01, ***p<0.001. Statistical significance was calculated by one-way ANOVA, followed by the Tukey post-hoc test). **D** Semi-quantitative analysis of mitochondria number (n=3. *p<0.05. Statistical significance was calculated by one-way ANOVA, followed by the Tukey post-hoc test). **E** Representative images for Mitotracker Red CMXRos staining. Scar bar (from top to bottom): 25 µm, 5 µm. **F** Seahorse analysis and **G** Basal respiration, ATP-linked respiration, and maximal respiration on MC3T3-E1 cells treatment with H₂O₂ or H₂O₂+CNs (n=5. **p<0.01, ***p<0.001. Statistical significance was calculated by one-way ANOVA, followed by the Tukey post-hoc test). **H** The activity of Caspase-3 after treatment in different groups (n=3. **p<0.01. Statistical significance was calculated by one-way ANOVA, followed by the Tukey post-hoc test). **I** Representative fluorescent images of TUNEL staining under different treatment conditions. Scar bar: 200 µm. **J** Flow cytometry apoptosis analysis and **K** quantitative analysis of apoptosis rate of different groups (n=3. ***p<0.001. Statistical significance was calculated by one-way ANOVA, followed by the Tukey post-hoc test). **L** qPCR analysis for mRNA levels of Bcl-2/Bax characterizes the degree of cell apoptosis (n=3. *p<0.05. Statistical significance was calculated by one-way ANOVA, followed by the Tukey post-hoc test). All data were presented as mean ± s.d.

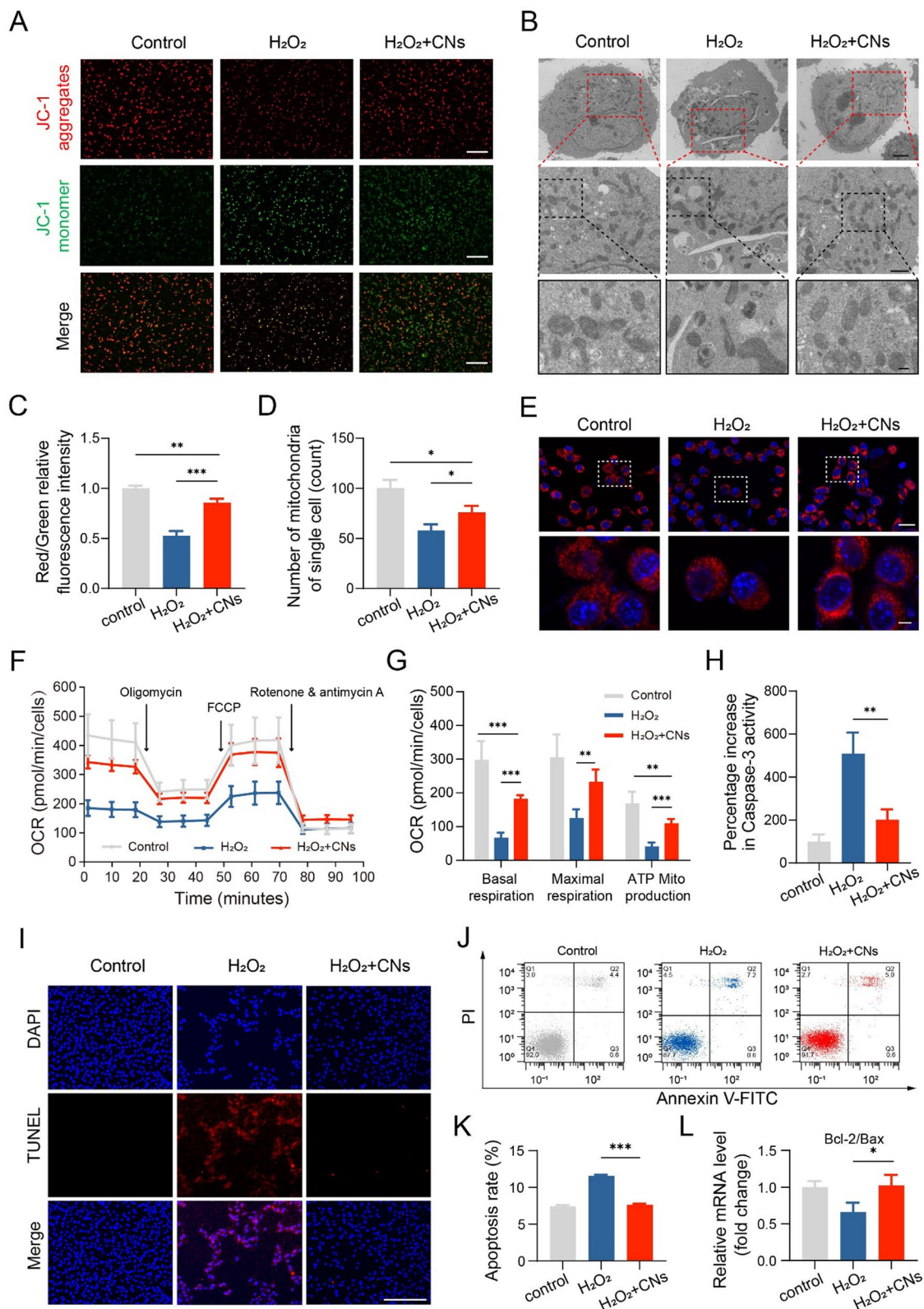


Fig. 3 (See legend on previous page.)

CNs demonstrated exceptional compatibility, with cell viability significantly increased compared with the H₂O₂ group, which indicated that multicomponent synergies and nanoparticulate effects enhanced cell compatibility. MCNs had moderate effects on ROS elimination and restoration of mitochondrial functions (Fig. 4F, G, Additional file 1: Fig. S31, S32). ALP staining image results revealed that individual Fru and QA molecules had minimal impact on ALP expression. In contrast, the MCNs group exhibited moderate ALP expression levels, while the CNs group demonstrated the highest ALP expression, attributable to the synergistic effects of multiple components (Fig. 4H, Additional file 1: Fig. S33). In addition, the degree of mineralization, as shown in Fig. 4I, followed this order: CNs > MCNs > QA > Fru (Additional file 1: Fig. S34, S35). As a result, CNs possessed excellent abilities to eliminate oxidative stress, restore osteoblast activity, and promote osteogenic differentiation through the synergistic effects of multiple active components.

RNA sequencing to analyze the cellular signaling mechanisms of CNs alleviate oxidative stress and restore osteoblast activity.

Next, we employed transcriptome RNA sequencing to elucidate the cellular signaling mechanisms by which CNs alleviate oxidative stress and restore osteoblast activity. As shown in Fig. 5A and B, a total of 4482 DEGs were identified between the H₂O₂ and control groups, with 2684 upregulated genes and 1798 downregulated genes. In the H₂O₂+CNs group compared to the H₂O₂ group, 563 genes were upregulated and 260 genes were downregulated. Then, the results of the GO functional enrichment analysis indicated that DEGs between H₂O₂ and control groups were predominantly enriched in processes related to cell differentiation, cell communication, biological regulation, and MAP kinase phosphatase activity (Fig. 5C, Additional file 1: Table. S4). Besides, the KEGG analysis showed that these genes were primarily associated with MAPK and calcium signaling pathways, which play important roles in oxidative stress response and bone regeneration (Fig. 5D). After treatment with CNs, GO analysis revealed that the DEGs between H₂O₂+CNs and H₂O₂ groups were mainly associated

with cell development, cell communication, calcium ion binding, and ion channel activity (Fig. 5E, Additional file 1: Table. S5), while KEGG results suggested that the calcium signaling pathway may play a crucial part in regulating oxidative stress and accelerating osteogenic differentiation (Fig. 5F, Additional file 1: Fig. S36, S37, and Table. S6). After normalizing to the control group, heat maps of DEGs associated with calcium and MAPK signaling pathways were generated to reveal the expression intensities. Many genes in the calcium signaling pathway (Fig. 5G), such as ATPase, Ca⁺⁺ transporting, plasma membrane (Atp2b), 5-hydroxytryptamine receptor 2A (Htr2a), and 5-hydroxytryptamine receptor 5A (Htr5a), were significantly down-regulated in the H₂O₂ group. However, treatment with CNs effectively reversed this downregulation. Recent studies have shown that high oxidative stress conditions can disrupt calcium homeostasis and induce apoptosis through the calcium signaling pathway [19, 63]. Therefore, we next examined intracellular calcium concentrations via a calcium colorimetric assay kit. Intracellular calcium concentrations increased significantly by 6.7 times following exposure to 1 mM H₂O₂, in comparison to the control group. However, the administration of 200 µg/mL CNs could reduce the intracellular calcium concentration (Fig. 5I). For the MAPK signaling pathway, oxidative stress in the H₂O₂ group induced the upregulation of dual specificity phosphatase 6 (Dusp6), Dusp10, and transformation-related protein 53 (Trp53) and promoted the downregulation of mitogen-activated protein kinase 10 (Mapk10). Nevertheless, CNs could protect cells from the harmful effects of oxidative stress on the MAPK signaling pathway, resulting in similar gene expression profiles between the CNs-treated and control groups (Fig. 5H). qPCR results found that stimulation of MC3T3-E1 cells with H₂O₂ led to upregulation of Dusp6 (4.1 fold), Dusp10 (40.5 fold), and Trp53 (2.1 fold), while the Mapk10 was downregulated to 28.8%. However, there were weaker expression changes in the above genes following the treatment of CNs, which well agreed with RNA sequencing results (Fig. 5J). In conclusion, CNs could reverse the influence of oxidative stress on calcium and MAPK signaling pathways, rebalance calcium homeostasis, and enhance osteoblast viability.

(See figure on next page.)

Fig. 4 Characterization and bioactivity evaluation of MCNs. **A** Schematic illustration of the synthesis of MCNs. **B** Size distribution and **C** zeta potential of MCNs (n = 3). **D** ABTS⁺ radical scavenging capacity of GMS, Fru, QA, MCNs, and CNs (n = 3. ***p < 0.001. Statistical significance was calculated by one-way ANOVA, followed by the Tukey post-hoc test). **E** Cell viability of MC3T3-E1 cells after treatment with different groups for 24 h under the condition of oxidative stress (n = 3. ***p < 0.001. Statistical significance was calculated by one-way ANOVA, followed by the Tukey post-hoc test). **F** Representative fluorescent images under different treatment conditions detected by JC-1 staining. Scar bar: 200 µm. **G** CLSM images of intracellular ROS in MC3T3-E1 cells under different treatment conditions stained by DCFH-DA. Scar bar: 50 µm. **H** ALP staining images and **I** ARS staining images of MC3T3-E1 cells after incubation with different groups with H₂O₂ stimulation. Scar bar: 100 µm. All data were presented as mean ± s.d.

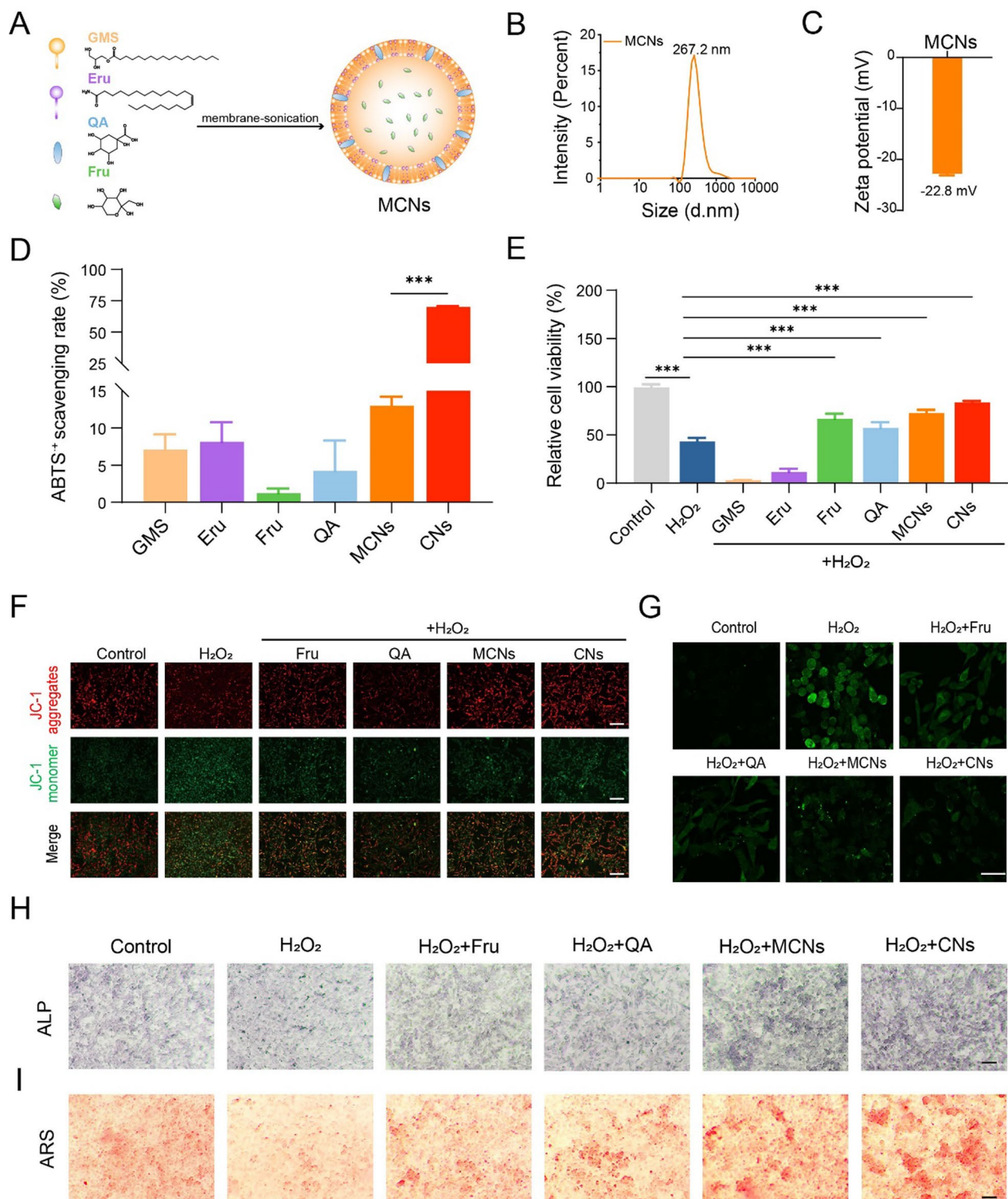


Fig. 4 (See legend on previous page.)

In vivo osteoporosis reversal

After confirming their robust antioxidant capacity and satisfactory osteogenic differentiation effects in vitro,

we proceeded to thoroughly assess the in vivo performance of CNs. We established the OVX model by surgically removing both ovaries from C57BL/6J mice for

subsequent studies [64, 65]. To visually investigate their in vivo fate, CNs were labeled with fluorescent dye DiO. After intravenous injection of D-CNs into the OVX model, the plasma drug concentration versus time profiles were shown in Additional file 1: Fig. S38 and S39, and the pharmacokinetic parameters were listed in Additional file 1: Table S7. CNs exhibited a long half-life period ($t_{1/2\beta}$, 37.2 h), with an area under the curve (AUC_{0-∞}) of 31.8 mg L⁻¹ h. DiR, a commercially available near-infrared fluorescent probe known for its powerful membrane affinity. The in vivo distribution of DiR-CN was visualized using a fluorescence imaging system. As shown in Fig. 6A, the DiR-CN group exhibited progressively stronger fluorescence in bone tissues over the 24-h treatment period. In contrast, the individual DiR molecules group displayed only a very weak fluorescence signal after up to 24 h of treatment. Quantitative analysis revealed that the fluorescence intensity at the femur and tibia sites in the DiR-CN group was 19.6-fold higher compared to the DiR group (Fig. 6B). These results fully suggested that CNs could passively target osteoporotic bone tissues due to the presence of noncontinuous bone marrow capillaries. Upon exposure to acidic osteoporotic microenvironment (pH 4.0), CNs undergo a transformation into larger particles. This change occurs due to alterations in surface charge driven by electrostatic interactions, which may potentially enhance their retention within bone tissue. Next, we evaluated the in vivo antioxidant properties and bone regeneration effects in the OVX mouse model. As shown in Fig. 6C, CNs were intravenously injected once every 3 days for 8 weeks. 17β-estradiol, a commonly used clinical osteoporosis drug, was selected as a positive control group for in vivo study. After 8 weeks, bone tissues were collected and stained for ROS using a DHE fluorescence probe. The ROS fluorescence intensity was higher in the OVX model group compared to the sham group, indicating enhanced oxidative stress in the microenvironment associated with osteoporosis. After treatment with 2.5 mg/kg CNs, the ROS level significantly decreased compared to the OVX group, which was consistent with previous results (Additional file 1: Fig. S40, S41). After confirming strong antioxidant capacity, we proceeded

to observe bone regeneration using micro-CT and 3D reconstruction (Fig. 6D). Cross-sectional 2D images and 3D reconstruction images displayed severe bone loss in the OVX mice. However, better connectivity and organized architecture of the trabecular bone were observed after CNs treatment, resembling the results seen in the E₂-positive group. In the quantitative results (Fig. 6E–I), the CNs group exhibited values of BV/TV (%), BMD (g cm⁻³), Tb. N (mm⁻¹), Tb. Th (mm), and Tb. Sp (mm) of 7.0%, 0.16 g cm⁻³, 1.37 mm⁻¹, 0.05 mm, and 0.29 mm, respectively. Moreover, no significant difference was observed between the CNs group and the sham group. Nevertheless, the OVX model group demonstrated lower values of BV/TV (3.6%), BMD (0.11 g cm⁻³), Tb. N (0.87 mm⁻¹), and Tb. Th (0.04 mm), as well as a higher value of Tb.Sp (0.36 mm). Meanwhile, the serum concentration ratio of bone formation-related marker calcium to phosphorus (Ca/P) also showed the same trend between the different groups (Fig. 6J). Notably, CNs have shown enormous potential as nanoantioxidants in terms of bone tissue retention and reversing osteoporosis.

To investigate the impact of CNs on bone metabolism, femoral tissues underwent detailed analysis using H&E staining as well as Masson staining. As shown in Fig. 7A, thin and loosely arranged microarchitectures were observed in the OVX model. As anticipated, the femoral tissues exhibited increased density and compactness following the CNs treatment regimen. Furthermore, Masson trichrome staining revealed a prominent osteoid matrix and decreased presence of lipid droplets in the CNs group (Fig. 7B). After the treatment period of 8 weeks, the administration of CNs resulted in a significant decrease in Dusp10-positive cells, showing a 2.5-fold reduction compared to the OVX group (Fig. 7C, D). More importantly, the number of JNK-positive cells was significantly increased compared to the OVX group (Fig. 7E, F). These results suggested that CNs counteracted bone loss in osteoporosis by regulating the microenvironment through the MAPK signaling pathway.

Last but not least, we thoroughly evaluated the biosafety of CNs, as excellent biocompatibility is crucial for their application in translational medicine. As shown

(See figure on next page.)

Fig. 5 Cellular signaling mechanisms of CNs alleviate oxidative stress and restore osteoblast activity. **A** Venn plot showing differential gene expression among groups. **B** Volcano map of DEGs about H₂O₂ vs control, H₂O₂ + CNs vs H₂O₂. **C** GO circle enrich diagram and **D** KEGG enrichment bubble diagram of DEGs and pathways between H₂O₂ and control. **E** GO and **F** KEGG enrichment analysis of DEGs and pathways between H₂O₂ + CNs and H₂O₂ (BP: Biological Process; CC: Cell Component; MF: Molecular Function). The ID information of the GO term is reported in detail in supplementary Table S4 and S5 in the Additional file 1. **G** Differential gene expression profiles of calcium signaling pathway and **H** MAPK signaling pathway among three groups (n = 3). **I** Intracellular calcium concentrations of MC3T3-E1 cells with different treatments normalized relatively to protein concentrations per well (n = 3. ***p < 0.001. Statistical significance was calculated by one-way ANOVA, followed by the Tukey post-hoc test). **J** qPCR analysis for mRNA levels of Dusp6, Dusp10, Mapk10, and Trp53 (n = 3. *p < 0.05. Statistical significance was calculated by one-way ANOVA, followed by the Tamhane post-hoc test). All data were presented as mean ± s.d.

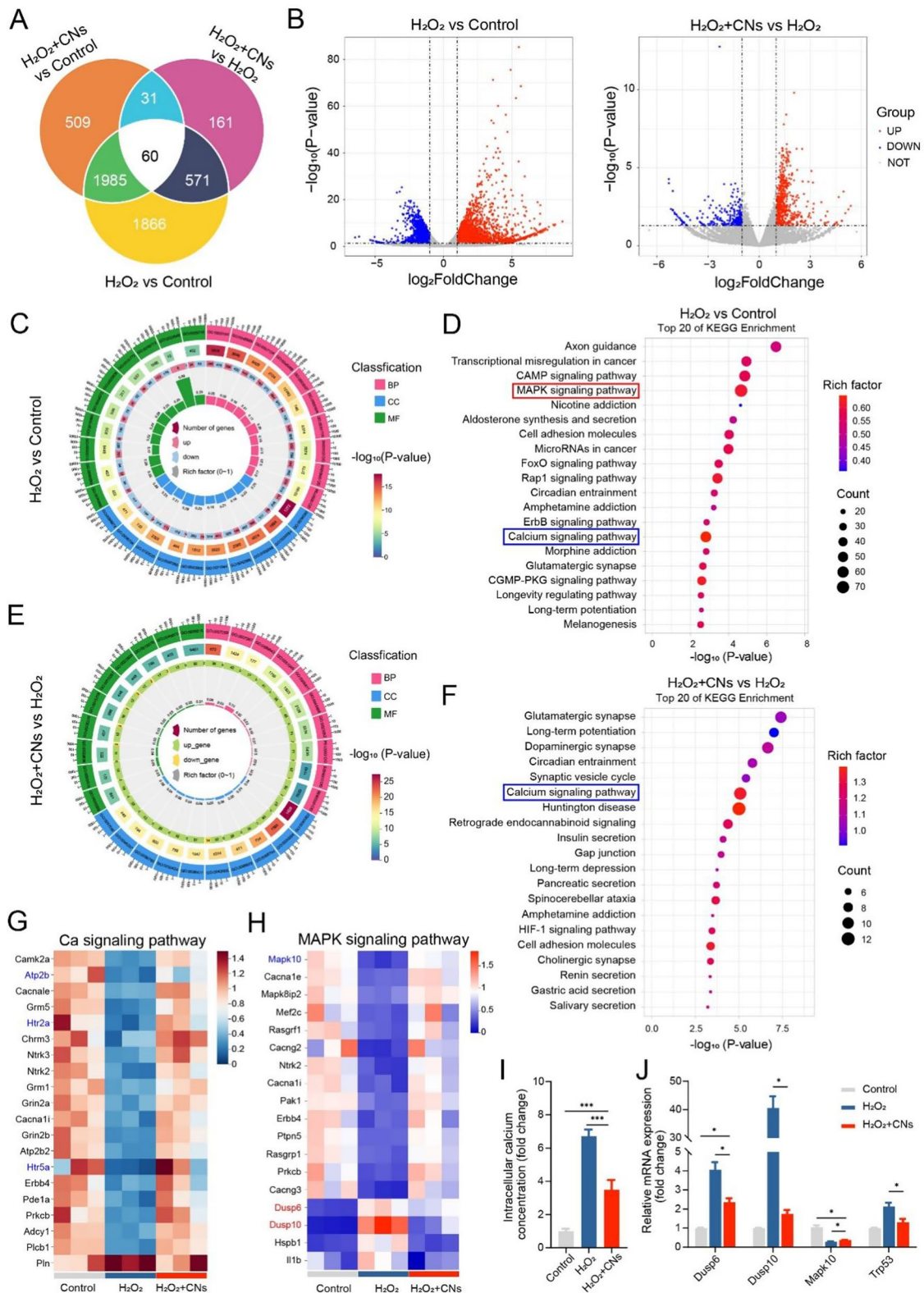


Fig. 5 (See legend on previous page.)

in Fig. 8A–D, the body weights increased from 18.2 to 24.0 g after treatment with 2.5 mg/kg of CNs. The results of the *in vivo* blood routine examination revealed that all key hematological parameters in the mice showed negligible changes (Fig. 8E). There were no significant fluctuations in liver functional indexes (ALT and AST) and kidney functional indicators (BUN and CREA) between the CNs-treated group and the sham group (Fig. 8F–I). H&E staining images disclosed that CNs had no significant effect on the major organs, including the heart, liver, spleen, lung, and kidney (Fig. 8J). In consequence, nanovesicles derived from carrots possessed good biocompatibility, offering huge potential in the treatment of osteoporosis and other biomedical applications.

Conclusion

In summary, we successfully constructed nanovesicles derived from carrots as a novel type of nanoantioxidants to modulate the oxidative stress microenvironment, thereby aiding in the reversal of bone rarefaction. Nanovesicles were obtained with well-defined

bilayer membrane structures, enriched with active ingredients. Nanovesicles demonstrated excellent dispersion under normal physiological conditions with significant stealth ability. However, at pH 4.0 mimicking an acidic osteoporotic microenvironment, they aggregated into larger particles, enhancing their retention within osteoporotic bone tissue. The nanovesicles effectively scavenged ROS and relieved oxidative stress, therapy restoring the mitochondrial function and osteogenic differentiation of osteoblast *in vitro*. Furthermore, nanovesicles could passively target and aggregate in bone tissue after an extended period in the bloodstream, which could help alleviate oxidative stress and reverse bone loss *in vivo*. Next, we aim to conduct an in-depth study comparing the efficacy and safety of these nanovesicles with existing treatments, such as bisphosphonates, estrogen, and calcium. This work presents the first demonstration of nanovesicles derived from carrots as innovative nanoantioxidants with the potential to promote osteogenesis, offering significant promise for clinical applications in osteoporosis treatment.

(See figure on next page.)

Fig. 6 *In vivo* distribution and promotion of osteogenesis in ovariectomized mice by tail vein injection of CNs. **A** Living fluorescence imaging of C57BL/6J mice's whole body and various tissues, including heart, liver, spleen, lung, kidney, and bone, after intravenous injection of PBS, DiR, and DiR-CN for 24 h. **B** DiR dye intensity was measured using the Living Image software ($n=3$, $***p < 0.001$). Statistical significance was calculated by one-way ANOVA, followed by the Tukey post-hoc test). **C** Schematic diagram of the establishment of animal models and treatment procedure. **D** Representative images of 3D micro-CT images of the structure of metaphyseal trabecular bone in the distal femur showing bone loss in OVX mice and regaining of bone mass by treatment with 2.5 mg/kg CNs. The areas magnified displayed the cross-section in 2D vision and partial bone volume in 3D vision, respectively. **E–I** Quantification of BV/TV (%), BMD (g cm^{-3}), Tb. N (mm^{-1}), Tb. Th (mm), and Tb. Sp (mm, $n=3$. $*p < 0.05$, $**p < 0.01$, NS, not significant. Statistical significance was calculated by one-way ANOVA, followed by the Tukey post-hoc test). **J** The serum concentration ratio of bone formation-related marker calcium to phosphorus in different groups ($n=3$. $*p < 0.05$, NS, not significant. Statistical significance was calculated by one-way ANOVA, followed by the Tukey post-hoc test). All data were presented as mean \pm s.d.

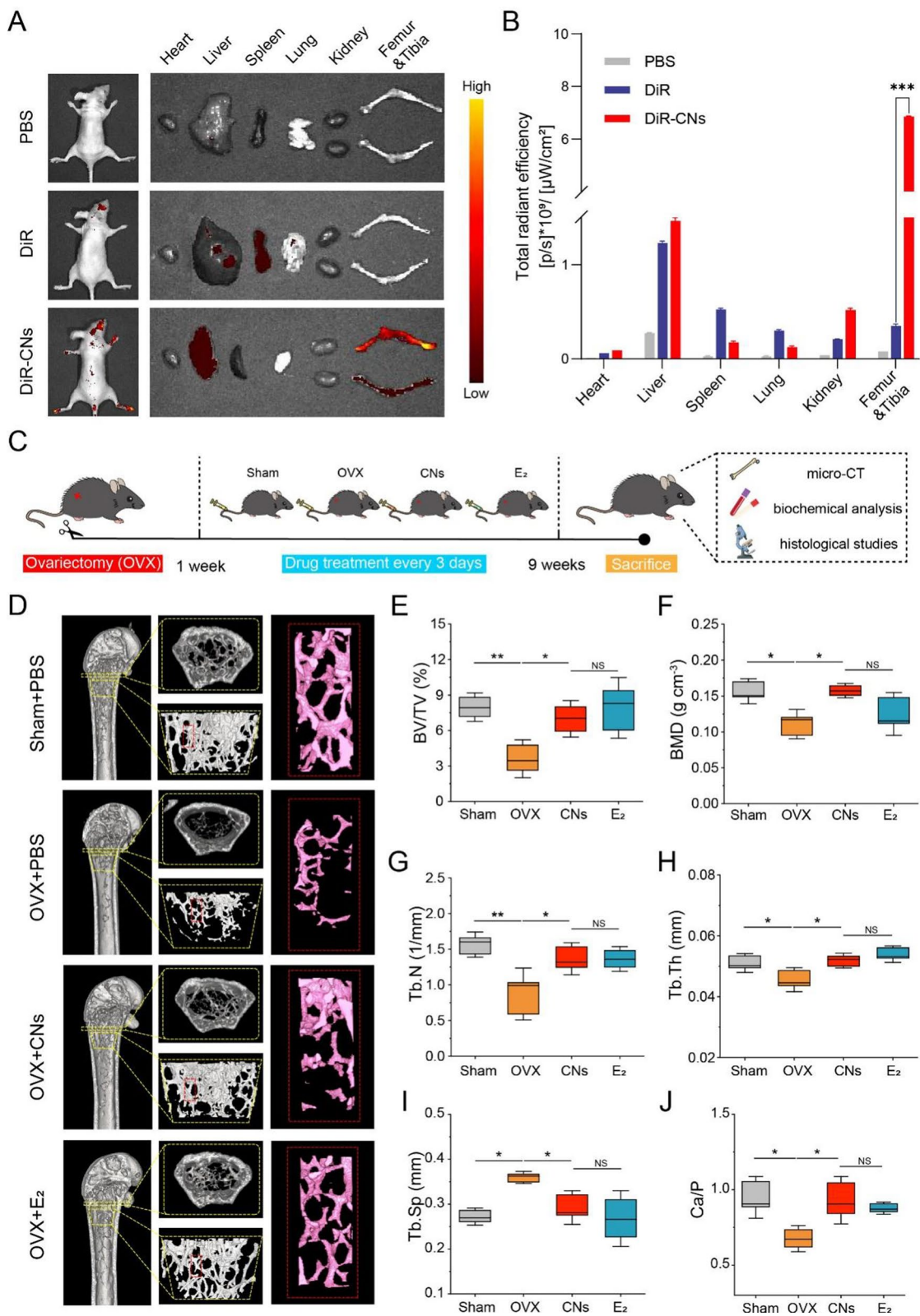


Fig. 6 (See legend on previous page.)

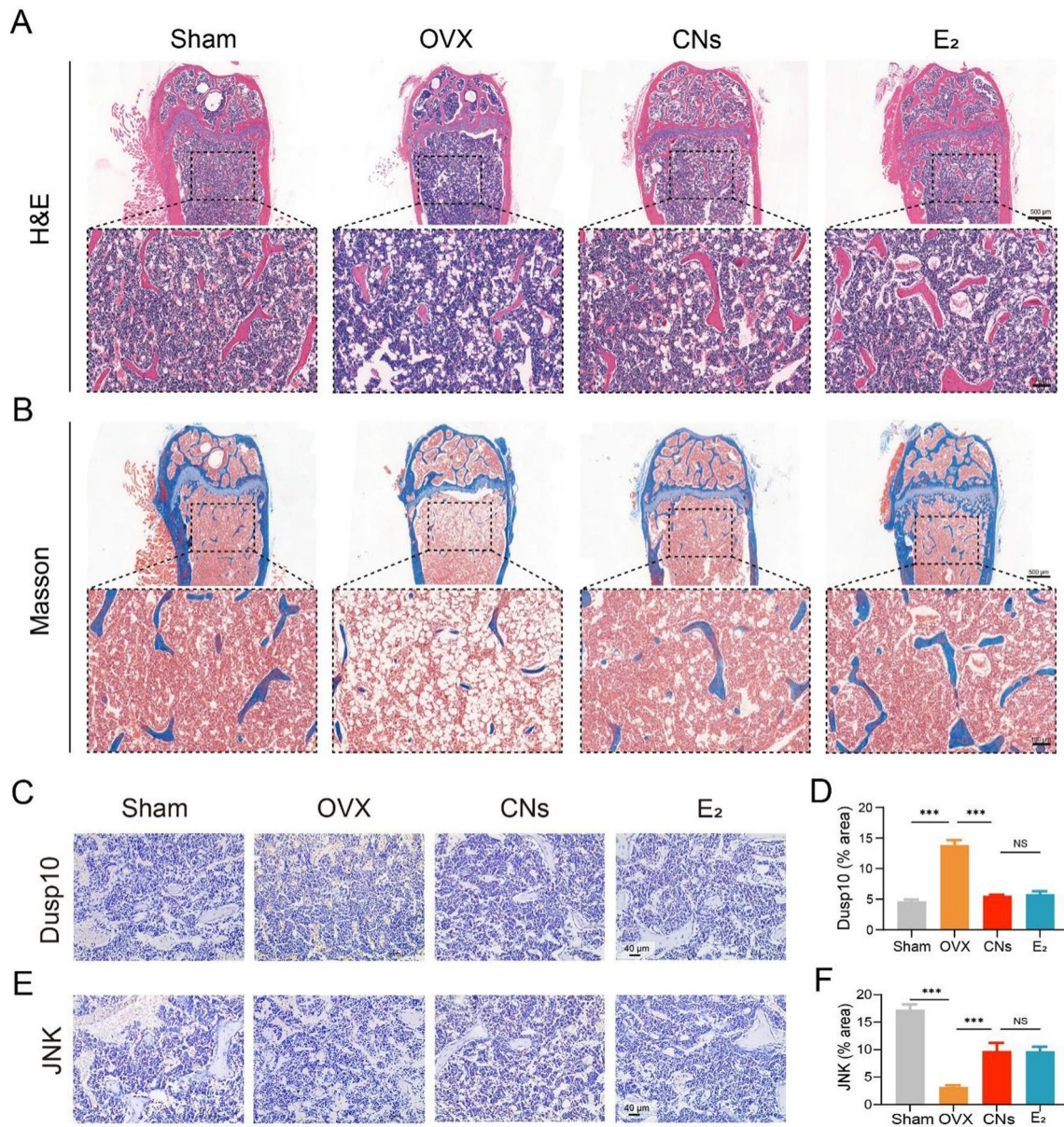


Fig. 7 Histological and immunohistochemical analysis. Representative images of **(A)** H&E and **(B)** Masson staining images of decalcified femoral sections. Scar bar: 500, 100 μm. Immunohistochemical images of decalcified femoral sections for **(C)** Dusp10 and **(E)** JNK protein in different groups. Scar bar: 40 μm. Semi-quantitative analysis of positively stained areas of **(D)** Dusp10 and **(F)** JNK in different groups (n = 3, ***p < 0.001. NS, not significant. Statistical significance was calculated by one-way ANOVA, followed by the Tukey post-hoc test). All data were presented as mean ± s.d.

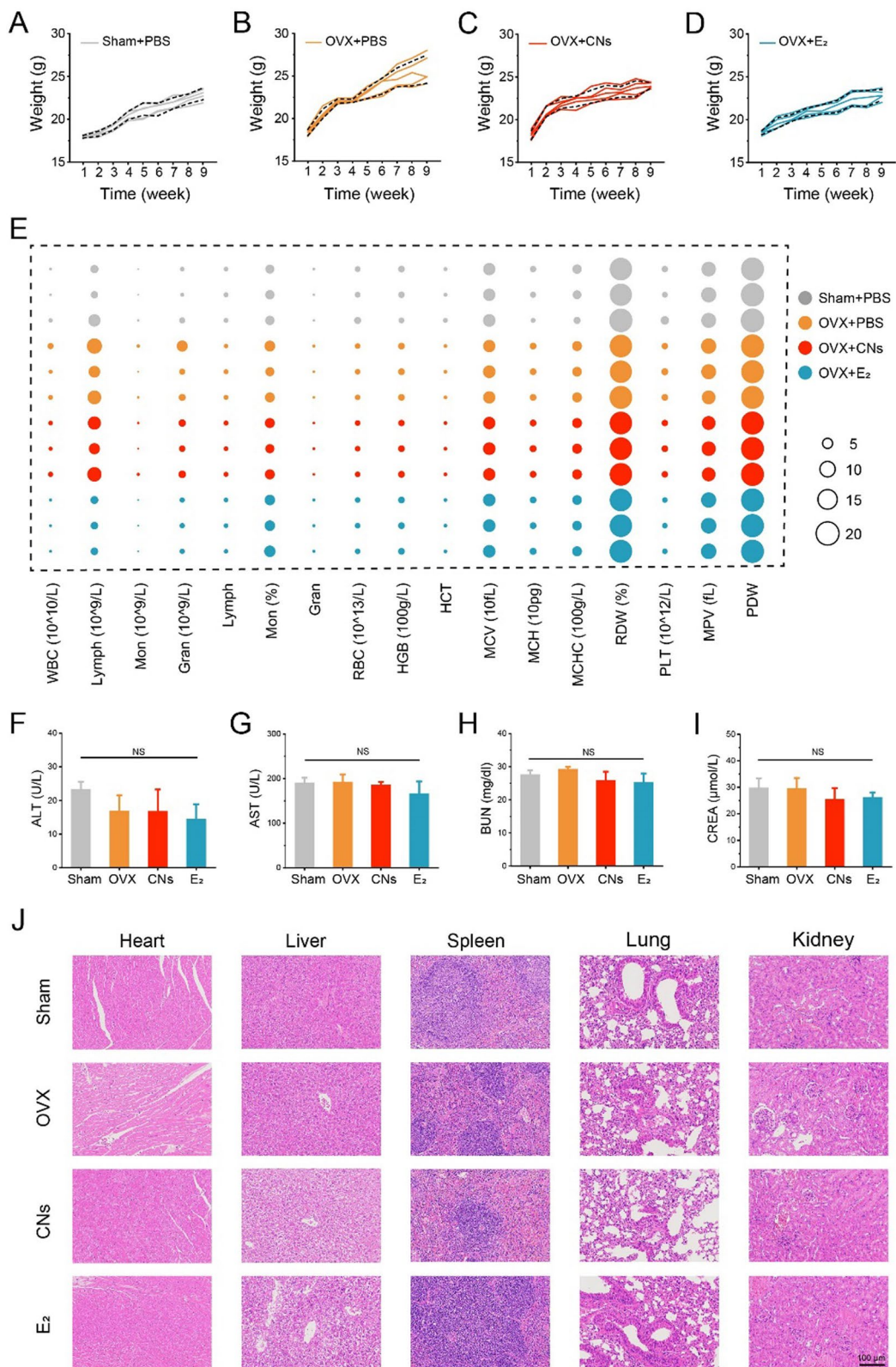


Fig. 8 In vivo safety evaluation. **A–D** Body weight of mice in different treatment groups over 8 weeks (n=5). **E** Routine blood tests of mice from different treatment groups 8 weeks after surgery (n=3). **F–I** ALT, AST, BUN, and CREA of mice from different treatment groups (n=3). NS, not significant. Statistical significance was calculated by one-way ANOVA, followed by the Tukey post-hoc test). **J** Histological images of the heart, liver, spleen, lung, and kidney of mice from different groups at 8 weeks postoperatively. Scar bar: 100 μm. All data were presented as mean ± s.d.

Abbreviations

ROS	Reactive oxygen species
·OH	Hydroxyl radicals
H ₂ O ₂	Hydrogen peroxide
O ₂ ^{·-}	Superoxide anion
CNs	Carrot-derived nanoantioxidants
MAPK	Mitogen-activated protein kinase
Eru	Erucamide
Fru	Fructose
QA	Quinic acid
DCFH-DA	2,7-Dichlorofluorescein diacetate
ALP	Alkaline phosphatase
DiO	3, 3'-Diocadecyloxycarbocyanine perchlorate
MitoTracker Red CMXRos	Mitochondria tracker red chloromethyl-X-rosamine
DiR	Exosome fluorescent labeling dye
ARS	Alizarin red S
DHE	Dihydroethidium
SOD	Superoxide dismutase
GMS	Glycerol monostearate
T-AOC	Total antioxidant activity
TUNEL	Terminal deoxynucleotidyl transferase 2-deoxyuridine 5-triphosphate nick end labeling
qPCR	Quantitative polymerase chain reaction
DMEM	Dulbecco's modified eagle medium
FBS	Fetal bovine serum
H&E	Hematoxylin and eosin
HRP	Horseradish peroxidase
Dusp10	Dual specificity phosphatase 10
JNK	Jun N-terminal kinases Polyclonal antibody
PBS	Phosphate buffer solution
DLS	Dynamic light scattering
TEM	Transmission electron microscopic
NTA	Nanoparticle tracking analysis
CEs	Carrot-derived exosomes
SDS-PAGE	Sodium dodecyl sulfate-polyacrylamide gel electrophoresis
DIA	Data-independent acquisition
GO	Gene ontology
KEGG	Kyoto encyclopedia of genes and genomes
UHPLC-Q-TOF-MS	Ultrahigh-performance liquid chromatography equipped with quadrupole time-of-flight mass spectrometry
MCNs	Mimic CNs
CAT	Catalase
O ₂	Oxygen
ABTS ⁺	2, 2'-Azino-bis (3-ethylbenzthiazoline-6-sulfonic acid) diammonium salt
D-CNs	DiO-loaded CNs
CLSM	Confocal laser scanning microscopy
JC-1	5, 5', 6, 6'-Tetrachloro-1, 1', 3, 3'-tetraethyl-imidacarbocyanine iodide
FCCP	Carbonyl Cyanide 4-(Trifluoromethoxy) phenylhydrazone
OCR	Oxygen consumption rate
PI	Propidium iodide
DEGs	Differentially expressed genes
DiR-CNs	DiR-loaded CNs
OVX	Ovariectomized
SPF	Specific pathogen-free
E ₂	17β-Estradiol
Micro-CT	Micro-computed tomography
BV/TV	Bone volume fraction
Tb. Th	Trabecular thickness
Tb. N	Trabecular number
Tb. Sp	Trabecular spacing
BMD	Bone mineral density
EDTA	Ethylenediaminetetraacetic acid
BSA	Bovine serum albumin
ALT	Alanine transaminase

AST	Aspartate aminotransferase
BUN	Blood urea nitrogen
CREA	Creatinine
Ca	Calcium
P	Phosphorus
ANOVA	Analysis of variance
s.d.	Standard deviation
Runx2	Runt-related transcription factor 2
OPN	Osteopontin
OCN	Osteocalcin
ΔΨ _m	Mitochondrial membrane potential
Bax	BCL2-associated X
Bcl-2	B-cell lymphoma-2
Atp2b	ATPase, Ca + + transporting, plasma membrane
Htr2a	5-Hydroxytryptamine receptor 2A
Htr5a	5-Hydroxytryptamine receptor 5A
Dusp6	Dual specificity phosphatase 6
Trp53	Transformation-related protein 53
Mapk10	Mitogen-activated protein kinase 10

Supplementary Information

The online version contains supplementary material available at <https://doi.org/10.1186/s12951-025-03235-y>.

Additional file 1: Fig. S1. TEM image of CNs. Scar bar: 500 nm. **Fig S2.** Zeta potential of CNs under different pH conditions including PBS (pH 7.4 and 4.0) at different times (n = 3). **Fig S3.** Protein concentrations in various batches of CNs (n = 3). **Fig S4.** Protein content of CNs under different storage temperatures (4, -20, and -80°C) for 2 weeks (n = 3). **Fig S5.** Size of CNs under different storage temperatures (4, -20, and -80°C) for 2 weeks (n = 3). **Fig S6.** Zeta potential of CNs under different storage temperatures (4, -20, and -80°C) for 2 weeks (n = 3). **Fig S7.** Characterization of CEs. **Fig S8.** SDS-PAGE of total proteins in the CNs. **Fig S9.** KEGG enrichment analysis of CNs proteins. **Fig S10.** GO enrichment analysis of CNs proteins. **Fig S11.** Pie chart of the proportion of the number of identified superclass metabolites of CNs in each chemical category. **Fig S12.** The relative percentage content of CNs superclass metabolites in each chemical category. **Fig S13.** Digital photos for the color change of O₂^{·-} cleared by different concentrations (from left to right: 0, 50, 100, 200, 400, 800, and 1600 µg/mL) of CNs. **Fig S14.** The absorbance shift (ΔA) between different concentrations of CNs and the control group at 550 nm. **Fig S15.** Photographs of time-dependent catalytic oxygen bubble formation after incubation of different CNs in H₂O₂ (2 mM). **Fig S16.** Digital photos for the color change of ABTS⁺ production were inhibited by various concentrations (from left to right: 0, 50, 100, 200, 400, 800, and 1600 µg/mL) of CNs. **Fig S17.** The absorbance shift (ΔA) at 734 nm represents the capacity of CNs to inhibit ABTS⁺ production. **Fig S18.** ABTS⁺ radical scavenging capacity at different concentrations of CNs (n = 3). **Fig S19.** Flow cytometry images of DiO cellular uptake at different times. **Fig S20.** Mean fluorescence intensity of DiO cellular uptake at different times (n = 3). **Fig S21.** The survival rate of MC3T3-E1 cells incubated with different concentrations of H₂O₂ for 3 h (n = 5). **Fig S22.** The survival rate of MC3T3-E1 cells incubated with different concentrations of H₂O₂ for 6 h (n = 5). **Fig S23.** The survival rate of MC3T3-E1 cells incubated with different concentrations of H₂O₂ for 24 h (n = 5). **Fig S24.** ALP staining images of MC3T3-E1 cells after incubation with different concentrations of CNs. Scar bar: 100 µm. **Fig S25.** Semi-quantitative statistics of ALP expression positive area of MC3T3-E1 cells on day 3 after treatment with CNs (n = 3). **Fig S26.** ARS staining images of MC3T3-E1 cells after incubation with different concentrations of CNs. Scar bar: 100 µm. **Fig S27.** Semi-quantitative statistics of mineralized nodules of MC3T3-E1 cells on day 5 after treatment with CNs (n = 3). **Fig S28.** Representative fluorescent images of JC-1 staining in the control group. Scar bar: 200 µm. **Fig S29.** Representative fluorescent images of JC-1 staining in the H₂O₂ group. Scar bar: 200 µm. **Fig S30.** Representative fluorescent images of JC-1 staining in the H₂O₂ + CNs group. Scar bar: 200 µm. **Fig S31.** Semi-quantitative analysis of red/green relative fluorescence intensity (n = 3. **p < 0.01, ***p < 0.001. Statistical significance was calculated by one-way ANOVA, followed by the Tukey post-hoc test). **Fig**

S32. Semi-quantitative analysis of intracellular ROS fluorescence intensity ($n = 3$, $***p < 0.001$). Statistical significance was calculated by one-way ANOVA, followed by the Tukey post-hoc test). **Fig S33.** Semi-quantitative statistics of ALP expression positive area of MC3T3-E1 cells on day 3 ($n = 3$, $**p < 0.01$, $***p < 0.001$). Statistical significance was calculated by one-way ANOVA, followed by the Tukey post-hoc test). **Fig S34.** ARS staining images of MC3T3-E1 cells after incubation with different groups with H_2O_2 stimulation. Scar bar: 100 μm . **Fig S35.** Semi-quantitative statistics of mineralized nodules of MC3T3-E1 cells on day 5 after treatment with Fru, QA, MCNs, and CNs under conditions of oxidative stress ($n = 3$, $***p < 0.001$). Statistical significance was calculated by one-way ANOVA, followed by the Tukey post-hoc test). **Fig S36.** GO circle enrich diagram of DEGs and pathways between $H_2O_2 + CNs$ and control groups. **Fig S37.** KEGG enrichment bubble diagram of DEGs and pathways between $H_2O_2 + CNs$ and control groups. **Fig S38.** Standard curve of DiO fluorescence intensity versus concentration in plasma. **Fig S39.** In vivo pharmacokinetics of D-CNs after intravenous injection into mice ($n = 3$). **Fig S40.** Representative images of bone tissue sections showing ROS fluorescence in various groups. **Fig S41.** Semi-quantitative statistics of DHE fluorescence intensity ($n = 3$, $***p < 0.001$). Statistical significance was calculated by one-way ANOVA, followed by the Tukey post-hoc test). **Table S1.** The content of main components in CNs relative to their mass. **Table S2.** The RIN values of RNA from different groups of samples were determined by an Agilent Bioanalyzer 4150 system. % Integrated Area (18S/28S) indicates the peak area of the 18S/28S subunit as a percentage of the total area. **Table S3.** Primer sequences used for qPCR. **Table S4.** The ID information of the GO term and the classification name corresponding to this ID of GO enrichment analysis between H_2O_2 and control groups. BP: Biological Process; CC: Cell Component; MF: Molecular Function. **Table S5.** The ID information of the GO term and the classification name corresponding to this ID of GO enrichment analysis between $H_2O_2 + CNs$ and H_2O_2 groups. **Table S6.** The ID information of the GO term and the classification name corresponding to this ID of GO enrichment analysis between $H_2O_2 + CNs$ and control groups. **Table S7.** Pharmacokinetic parameters of D-CNs ($n = 3$).

Author contributions

X. Zhang, M. Lee, Y. Feng, and R. Hou guided the project; J. Peng, R. Liu, D. Chen, and Z. Chang performed the experiments; J. Peng, J. Xu, Y. Yao, B. Li, and R. Zhao analyzed the data and prepared figures; J. Peng, X. Zhang, M. Lee, and Y. Feng wrote the manuscript. All authors reviewed the manuscript.

Funding

This work was supported by the National Natural Science Foundation of China (82102207), the Research Project established by Chinese Pharmaceutical Association Hospital Pharmacy Department (CPA-Z05-ZC-2024002), the Open Fund from Key Laboratory of Cellular Physiology, Shanxi Medical University (CPOF202303), the Natural Science Foundation of Shanxi Province (20210302124036), the Shanxi Province Higher Education "Billion Project" Science and Technology Guidance Project (BYJL059), and the Special Fund from Medicinal Basic Research Innovation Center of Chronic Kidney Disease, Ministry of Education, Shanxi Medical University (CKD/SXMU-2024-03).

Availability of data and materials

No datasets were generated or analysed during the current study.

Declarations

Ethics approval and consent to participate

All animal experiments were approved by the Ethics Committee Second Hospital of Shanxi Medical University with the approval number (DW2023040).

Consent for publication

All authors agreed to submit this manuscript.

Competing interests

The authors declare no competing interests.

Author details

¹Second Clinical Medical College, School of Pharmacy and Key Laboratory of Cellular Physiology, Shanxi Medical University, Taiyuan, Shanxi 030001, People's Republic of China. ²Division of Advanced Prosthodontics, University of California at Los Angeles, Los Angeles, CA 90095, USA. ³Shanxi Provincial Key Laboratory of Cellular Physiology, Shanxi Medical University, Taiyuan, Shanxi 030001, People's Republic of China. ⁴Medicinal Basic Research Innovation Center of Chronic Kidney Disease, Ministry of Education, Shanxi Medical University, Taiyuan, Shanxi 030001, People's Republic of China.

Received: 10 September 2024 Accepted: 16 February 2025

Published online: 12 March 2025

References

- Luhmann T, Germershaus O, Groll J, Meinel L. Bone targeting for the treatment of osteoporosis. *J Control Release*. 2012;161:198–213.
- Yu B, Wang C. Osteoporosis: the result of an 'Aged' bone microenvironment. *Trends Mol Med*. 2016;22:641–4.
- Lei C, Song J, Li S, Zhu Y, Liu M, Wan M, Mu Z, Tay FR, Niu L. Advances in materials-based therapeutic strategies against osteoporosis. *Biomaterials*. 2023;296: 122066.
- Zhivodernikov IV, Kirichenko TV, Markina YV, Postnov AY, Markin AM. Molecular and cellular mechanisms of osteoporosis. *Int J Mol Sci*. 2023;24:15772.
- Ensrud KE, Crandall CJ. Osteoporosis. *Ann Intern Med*. 2017;167:17–32.
- Khosla S, Hofbauer LC. Osteoporosis treatment: recent developments and ongoing challenges. *Lancet Diabetes Endo*. 2017;5:898–907.
- Reid IR, Billington EO. Drug therapy for osteoporosis in older adults. *Lancet*. 2022;399:1080–92.
- Zhao M, Kang M, Wang J, Yang R, Zhong X, Xie Q, Zhou S, Zhang Z, Zheng J, Zhang Y, et al. Stem cell-derived nanovesicles embedded in dual-layered hydrogel for programmed ROS regulation and comprehensive tissue regeneration in burn wound healing. *Adv Mater*. 2024;36: e2401369.
- Ding L, Chen Y, Zhang B, Hu R, Dai C, Dong C, Huang H. Living macrophage-delivered tetrapod PdH nanoenzyme for targeted atherosclerosis management by ROS scavenging, hydrogen anti-inflammation, and autophagy activation. *ACS Nano*. 2022;16:15959–76.
- Yang W, Li K, Pan Q, Huang W, Xiao Y, Lin H, Liu S, Chen X, Lv X, Feng S, et al. An engineered bionic nanoparticle sponge as a cytokine trap and reactive oxygen species scavenger to relieve disc degeneration and discogenic pain. *ACS Nano*. 2024;18:3053–72.
- Yang L, Bhujel B, Hou Y, Luo J, An SB, Han I, Lee KB. Effective modulation of inflammation and oxidative stress for enhanced regeneration of intervertebral discs using 3D porous hybrid protein nanoscaffold. *Adv Mater*. 2023;35: e2303021.
- Liu Y, Luo J, Liu Y, Liu W, Yu G, Huang Y, Yang Y, Chen X, Chen T. Brain-targeted biomimetic nanodecoys with neuroprotective effects for precise therapy of Parkinson's disease. *ACS Cent Sci*. 2022;8:1336–49.
- Zhang W, Ge Z, Xiao Y, Liu D, Du J. Antioxidant and immunomodulatory polymer vesicles for effective diabetic wound treatment through ROS scavenging and immune modulating. *Nano Lett*. 2024;24:9494–504.
- Chen M, Wang D, Li M, He Y, He T, Chen M, Hu Y, Luo Z, Cai K. Nanocatalytic biofunctional MOF coating on titanium implants promotes osteoporotic bone regeneration through cooperative pro-osteoblastogenesis MSC reprogramming. *ACS Nano*. 2022;16:15397–412.
- Xu Y, Luo Y, Weng Z, Xu H, Zhang W, Li Q, Liu H, Liu L, Wang Y, Liu X, et al. Microenvironment-responsive metal-phenolic nanozyme release platform with antibacterial, ROS scavenging, and osteogenesis for periodontitis. *ACS Nano*. 2023;17:18732–46.
- Zhang D, Ji L, Yang Y, Weng J, Ma Y, Liu L, Ma W. Ceria nanoparticle systems alleviate degenerative changes in mouse postovulatory aging oocytes by reducing oxidative stress and improving mitochondrial functions. *ACS Nano*. 2024;18:13618–34.
- He Z, Sun C, Ma Y, Chen X, Wang Y, Chen K, Xie F, Zhang Y, Yuan Y, Liu C. Rejuvenating aged bone repair through multihierarchy reactive oxygen species-regulated hydrogel. *Adv Mater*. 2023;36:6552.

18. Han R, Wu Y, Han Y, Liu X, Liu H, Su J. Titania nanotube array supported nanoceria with redox cycling stability ameliorates oxidative stress-inhibited osteogenesis. *Chem Eng J*. 2024;17:2857–73.
19. Wang Y, Li X, Zhou S, Li J, Zhu Y, Wang Q, Zhao F. Zhou C-h: MCU inhibitor ruthenium red alleviates the osteoclastogenesis and ovariectomized osteoporosis via suppressing RANKL-induced ROS production and NFATc1 activation through P38 MAPK signaling pathway. *Oxid Med Cell Longev*. 2022;2022:1–27.
20. Gu J, Zhang P, Li H, Wang Y, Huang Y, Fan L, Ma X, Qian X, Xi J. Cerium–luteolin nanocomplexes in managing inflammation-related diseases by antioxidant and immunoregulation. *ACS Nano*. 2024;18:6229–42.
21. Li L, Wang Y, Xu Y, Xu J, Zhao Y, Cheng Z, Fang Y, Miao Y, Zhang X. ROS-scavenging lipid-based liquid crystalline as a favorable stem cell extracellular vesicles delivery vector to promote wound healing. *J Control Release*. 2024;371:298–312.
22. Bai L, Liu Y, Zhang X, Chen P, Hang R, Xiao Y, Wang J, Liu C. Osteoporosis remission via an anti-inflammatory effect by icariin activated autophagy. *Biomaterials*. 2023;297: 122125.
23. Chen Q, Qian Q, Xu H, Zhou H, Chen L, Shao N, Zhang K, Chen T, Tian H, Zhang Z, et al. Mitochondrial-targeted metal-phenolic nanoparticles to attenuate intervertebral disc degeneration: alleviating oxidative stress and mitochondrial dysfunction. *ACS Nano*. 2024;18:8885–905.
24. Liang X, Li Y, Guo B, Zeng Z, Deng K, Zou D, Xie Y, Xu Y, Shen C, Xu X. Inherent tumor microenvironment-reversing hydrogels: potentiating molecular therapy efficacy against drug-resistant tumors. *Adv Funct Mater*. 2024;34:2314772.
25. Qu Y, Meng B, Cai S, Yang B, He Y, Fu C, Li X, Li P, Cao Z, Mao X, et al. Apoptotic metabolites ameliorate bone aging phenotypes via TCOF1/FLVCR1-mediated mitochondrial homeostasis. *J Nanobiotechnol*. 2024;22:549.
26. Han R, Wu Y, Han Y, Liu X, Liu H, Su J. Engineered plant extracellular vesicles for autoimmune diseases therapy. *Nano Res*. 2023;17:2857–73.
27. Zhao B, Lin H, Jiang X, Li W, Gao Y, Li M, Yu Y, Chen N, Gao J. Exosome-like nanoparticles derived from fruits, vegetables, and herbs: innovative strategies of therapeutic and drug delivery. *Theranostics*. 2024;14:4598–621.
28. Kilasoniya A, Garaeva L, Shtam T, Spitsyna A, Putevich E, Moreno-Chamba B, Salazar-Bermeo J, Komarova E, Malek A, Valero M, Saura D. Potential of plant exosome vesicles from grapefruit (*Citrus x paradisi*) and tomato (*Solanum lycopersicum*) juices as functional ingredients and targeted drug delivery vehicles. *Antioxidants-Basel*. 2023;12:12040943.
29. Cong M, Tan S, Li S, Gao L, Huang L, Zhang HG, Qiao H. Technology insight: plant-derived vesicles-how far from the clinical biotherapeutics and therapeutic drug carriers? *Adv Drug Deliv Rev*. 2022;182: 114108.
30. Zheng L, Zhuang Z, Li Y, Shi T, Fu K, Yan W, Zhang L, Wang P, Li L, Jiang Q. Bone targeting antioxidant nano-iron oxide for treating postmenopausal osteoporosis. *Bioact Mater*. 2022;14:250–61.
31. Li J, Duan Q, Wei X, Wu J, Yang Q. Kidney-targeted nanoparticles loaded with the natural antioxidant rosmarinic acid for acute kidney injury treatment. *Small*. 2022;18: e2204388.
32. Long Y, Wei H, Li J, Li M, Wang Y, Zhang Z, Cao T, Carlos C, German LG, Jiang D, et al. Prevention of hepatic ischemia-reperfusion injury by carbohydrate-derived nanoantioxidants. *Nano Lett*. 2020;20:6510–9.
33. Pandey BK, Pandey KB, Srivastava SK. Chapter 19 -Uses of nanotechnology in refining the anti-aging activities of plant bioactives. In *Plant Bioactives as Natural Panacea Against Age-Induced Diseases*. Elsevier; 2023: 387–403.
34. Zu M, Xie D, Canup BSB, Chen N, Wang Y, Sun R, Zhang Z, Fu Y, Dai F, Xiao B. 'Green' nanotherapeutics from tea leaves for orally targeted prevention and alleviation of colon diseases. *Biomaterials*. 2021;279: 121178.
35. Zhang L, Li S, Cong M, Liu Z, Dong Z, Zhao M, Gao K, Hu L, Qiao H. Lemon-derived extracellular vesicle-like nanoparticles block the progression of kidney stones by antagonizing endoplasmic reticulum stress in renal tubular cells. *Nano Lett*. 2023;23:1555–63.
36. Xu X, Yuan T, Dad HA, Shi M, Huang Y, Jiang Z, Peng L. Plant exosomes as novel nanoplatforams for microRNA transfer stimulate neural differentiation of stem cells in vitro and in vivo. *Nano Lett*. 2021;21:8151–9.
37. Hwang JH, Park YS, Kim HS, Kim DH, Lee SH, Lee CH, Lee SH, Kim JE, Lee S, Kim HM, et al. Yam-derived exosome-like nanovesicles stimulate osteoblast formation and prevent osteoporosis in mice. *J Control Release*. 2023;79:184–98.
38. Chen X, He L, Zhang C, Zheng G, Lin S, Zou Y, Lu Y, Feng Y, Zheng D. Exploring new avenues of health protection: plant-derived nanovesicles reshape microbial communities. *J Nanobiotechnol*. 2024;22:269.
39. Liu J, Xiang J, Jin C, Ye L, Wang L, Gao Y, Lv N, Zhang J, You F, Qiao H, Shi L. Medicinal plant-derived mtDNA via nanovesicles induces the cGAS-STING pathway to remold tumor-associated macrophages for tumor regression. *J Nanobiotechnol*. 2023;21:78.
40. Han J, Wu T, Jin J, Li Z, Cheng W, Dai X, Yang K, Zhang H, Zhang Z, Zhang H, et al. Exosome-like nanovesicles derived from *Phellinus linteus* inhibit Mical2 expression through cross-kingdom regulation and inhibit ultraviolet-induced skin aging. *J Nanobiotechnol*. 2022;20:455.
41. Kim J, Li S, Zhang S, Wang J. Plant-derived exosome-like nanoparticles and their therapeutic activities. *Asian J Pharm SCI*. 2022;17:53–69.
42. Lian MQ, Chng WH, Liang J, Yeo HQ, Lee CK, Belaid M, Tollemeto M, Wacker MG, Czarny B, Pastorin G. Plant-derived extracellular vesicles: recent advancements and current challenges on their use for biomedical applications. *J Extracell Vesicles*. 2022;11: e12283.
43. Zeng L, Wang H, Shi W, Chen L, Chen T, Chen G, Wang W, Lan J, Huang Z, Zhang J, Chen J. Aloe derived nanovesicle as a functional carrier for indocyanine green encapsulation and phototherapy. *J Nanobiotechnol*. 2021;19:439.
44. Wang Q, Zhuang X, Mu J, Deng Z-B, Jiang H, Zhang L, Xiang X, Wang B, Yan J, Miller D, Zhang H-G. Delivery of therapeutic agents by nanoparticles made of grapefruit-derived lipids. *Nat Commun*. 2013;4:11347.
45. Shen W, Hsu RS, Fang J, Hu P, Chiang CS, Hu S. Marginative delivery-mediated extracellular leakiness and T cell infiltration in lung metastasis by a biomimetic nanoraspberry. *Nano Lett*. 2021;21:1375–83.
46. Niu W, Xiao Q, Wang X, Zhu J, Li J, Liang X, Peng Y, Wu C, Lu R, Pan Y, et al. A biomimetic drug delivery system by integrating grapefruit extracellular vesicles and doxorubicin-loaded heparin-based nanoparticles for glioma therapy. *Nano Lett*. 2021;21:1484–92.
47. Xiao Q, Zhao W, Wu C, Wang X, Chen J, Shi X, Sha S, Li J, Liang X, Yang Y, et al. Lemon-derived extracellular vesicles nanodrugs enable to efficiently overcome cancer multidrug resistance by endocytosis-triggered energy dissipation and energy production reduction. *Adv Sci*. 2022;9: e2105274.
48. Lu X, Xu Z, Shu F, Wang Y, Han Y, Yang X, Shi P, Fan C, Wang L, Yu F, et al. Reactive oxygen species responsive multifunctional fusion extracellular nanovesicles: prospective treatments for acute heart transplant rejection. *Adv Mater*. 2024;36: e2406758.
49. Kobaek-Larsen M, Deding U, Al-Najami I, Clausen BH, Christensen LP. Carrot juice intake affects the cytokine and chemokine response in human blood after ex vivo lipopolysaccharide-induced inflammation. *Nutrients*. 2023;15:5002.
50. Kim DK, Rhee WJ. Antioxidative effects of carrot-derived nanovesicles in cardiomyoblast and neuroblastoma cells. *Pharmaceutics*. 2021;13:1203.
51. Dou C, Li J, He J, Luo F, Yu T, Dai Q, Chen Y, Xu J, Yang X, Dong S. Bone-targeted pH-responsive cerium nanoparticles for anabolic therapy in osteoporosis. *Bioact Mater*. 2021;6:4697–706.
52. Lin X, Wang Q, Gu C, Li M, Chen K, Chen P, Tang Z, Liu X, Pan H, Liu Z, et al. Smart nanosacrificial layer on the bone surface prevents osteoporosis through acid-base neutralization regulated biocascade effects. *J Am Chem Soc*. 2020;142:17543–56.
53. Fu H, Wang L, Bao Q, Ni D, Hu P, Shi J. Acid neutralization and immune regulation by calcium-aluminum-layered double hydroxide for osteoporosis reversion. *J Am Chem Soc*. 2022;144:8987–99.
54. Fan J, Lee C-S, Kim S, Chen C, Aghaloo T, Lee M. Generation of small RNA-modulated exosome mimetics for bone regeneration. *ACS Nano*. 2020;14:11973–84.
55. Zhuang X, Deng ZB, Mu J, Zhang L, Yan J, Miller D, Feng W, McClain CJ, Zhang HG. Ginger-derived nanoparticles protect against alcohol-induced liver damage. *J Extracell Vesicles*. 2015;4:28713.
56. Chen H, Wang S, Zhang X, Hua X, Liu M, Wang Y, Wu S, He W. Pharmacological inhibition of RUNX1 reduces infarct size after acute myocardial infarction in rats and underlying mechanism revealed by proteomics implicates repressed cathepsin levels. *Funct Integr Genomics*. 2024;24:113.
57. Ou X, Wang H, Tie H, Liao J, Luo Y, Huang W, Yu R, Song L, Zhu J. Novel plant-derived exosome-like nanovesicles from *Catharanthus roseus*: preparation, characterization, and immunostimulatory effect via TNF- α /NF- κ B/PU.1 axis. *J Nanobiotechnol*. 2023;21:160.

58. Li M, Yu Y, Xue K, Li J, Son G, Wang J, Qian W, Wang S, Zheng J, Yang C, Ge J. Genistein mitigates senescence of bone marrow mesenchymal stem cells via ER α -mediated mitochondrial biogenesis and mitophagy in ovariectomized rats. *Redox Biol.* 2023;61: 102649.
59. Kim MK, Choi YC, Cho SH, Choi JS, Cho YW. The antioxidant effect of small extracellular vesicles derived from aloe vera peels for wound healing. *Tissue Eng Regen Med.* 2021;18:561–71.
60. Yang L, Li M, Sun Y, Zhang L. A cell-penetrating peptide conjugated carboxymethyl-beta-cyclodextrin to improve intestinal absorption of insulin. *Int J Biol Macromol.* 2018;111:685–95.
61. Yan R, Guo Y, Wang X, Liang G, Yang A, Li J. Near-infrared light-controlled and real-time detection of osteogenic differentiation in mesenchymal stem cells by upconversion nanoparticles for osteoporosis therapy. *ACS Nano.* 2022;16:8399–418.
62. Zhang X, Li Y, Hu C, Wu Y, Zhong D, Xu X, Gu Z. Engineering anticancer amphipathic peptide-dendronized compounds for highly-efficient plasma/organelle membrane perturbation and multidrug resistance reversal. *ACS Appl Mater Interfaces.* 2018;10:30952–62.
63. Teng C, Huang W, Meng T. Several dual specificity phosphatases coordinate to control the magnitude and duration of JNK activation in signaling response to oxidative stress. *J Biol Chem.* 2007;282:28395–407.
64. Chang Z, Chen D, Peng J, Liu R, Li B, Kang J, Guo L, Hou R, Xu X, Lee M, Zhang X. Bone-targeted supramolecular nanoagonist assembled by accurate ratiometric herbal-derived therapeutics for osteoporosis reversal. *Nano Lett.* 2024;24:5154–64.
65. Yang Y, Zheng Y, Liu J, Chang Z, Wang Y, Shao Y, Hou R, Zhang X. Natural chlorogenic acid-planted nanohybrids with steerable hyperthermia for osteosarcoma suppression and bone regeneration. *Adv Healthc Mater.* 2023;12:2300325.

Publisher's Note

Springer Nature remains neutral with regard to jurisdictional claims in published maps and institutional affiliations.